



All Theses and Dissertations

---

2017-07-01

# Ion Transport in a Commercial ICP-MS

Jessica Joline Larsen  
*Brigham Young University*

Follow this and additional works at: <https://scholarsarchive.byu.edu/etd>

 Part of the [Chemistry Commons](#)

---

## BYU ScholarsArchive Citation

Larsen, Jessica Joline, "Ion Transport in a Commercial ICP-MS" (2017). *All Theses and Dissertations*. 6905.  
<https://scholarsarchive.byu.edu/etd/6905>

This Thesis is brought to you for free and open access by BYU ScholarsArchive. It has been accepted for inclusion in All Theses and Dissertations by an authorized administrator of BYU ScholarsArchive. For more information, please contact [scholarsarchive@byu.edu](mailto:scholarsarchive@byu.edu), [ellen\\_amatangelo@byu.edu](mailto:ellen_amatangelo@byu.edu).

Ion Transport in a Commercial ICP-MS

Jessica Joline Larsen

A thesis submitted to the faculty of  
Brigham Young University  
in partial fulfillment of the requirements for the degree of

Master of Science

Paul B. Farnsworth, Chair  
Jaron C. Hansen  
Eric T. Sevy

Department of Chemistry and Biochemistry

Brigham Young University

Copyright © 2017 Jessica Joline Larsen

All Rights Reserved

## ABSTRACT

### Ion Transport in a Commercial ICP-MS

Jessica Joline Larsen  
Department of Chemistry and Biochemistry, BYU  
Master of Science

The performance of an inductively coupled plasma mass spectrometer, ICP-MS, depends on the instrument's ability to transport sample ions through the vacuum interface and focus the ions into a well-defined beam that will eventually reach the mass analyzer. In this study two main experiments were performed on the Perkin Elmer NexION 300S, a commercial ICP-MS. First, planar laser-induced fluorescence images were taken of the ion beam in a working instrument downstream from a unique quadrupole ion deflector. The images showed the ability of the instrument design to focus the ions in the ion beam. Second, laser-induced fluorescence was used to characterize ion flow through the vacuum interface. The interface is unique to the NexION ICP-MS in that there are three extraction cones. The effect of a three-cone interface on ideal skimming is discussed.

Keywords: ICP-MS, ion transport efficiency, laser-induced fluorescence

## ACKNOWLEDGEMENTS

I would like to acknowledge my research advisor and mentor Dr. Paul Farnsworth, and thank him for teaching me and letting me work in his group. The experiences I have had in your group have shaped me as a learner and provided many opportunities to stretch myself, for which I am grateful. I would also like to acknowledge by graduate committee Dr. Farnsworth, Dr. Hansen, and Dr. Sevy and thank them for their help as I have pursued a master's degree. I acknowledge Perkin Elmer and thank them for their financial support, and I would like to thank Dr. Hamid Badiei for his collaboration on the project. I also extend thanks to Dr. Bergeson for all of his help on the laser system, and Dr. Macedone for his help with LabVIEW. My lab members have been amazing to work with, and I would like to thank Alisa Edmund for training me on this project as an undergraduate student. I acknowledge and thank the BYU Department of Chemistry and Biochemistry and the J. Rex and Marcia A Goates Fellowship for their financial support. Finally, I would like to acknowledge my family members who have helped me along the way. Thanks Mom and Dad for teaching me the importance of education and of hard work. Thank you to my sister Jennifer, who has helped support me in various ways, and to all of my siblings for their love and support. A very special thanks to my husband Jacob, who has continually encouraged me to work hard and has supported my education goals.

## TABLE OF CONTENTS

ABSTRACT.....	ii
TABLE OF CONTENTS.....	iv
LIST OF TABLES.....	vi
LIST OF FIGURES.....	vii
1 Introduction.....	1
1.1 ICP-MS Overview.....	1
1.1.1 ICP-MS Principle of operation.....	2
1.2 ICP-MS Limitations.....	4
1.2.1 Space Charge Effects.....	4
1.2.2 Sampling Efficiency.....	6
1.3 Background.....	6
1.3.1 Planar Laser Induced Fluorescence Second Vacuum Stage Studies.....	7
1.3.2 Laser Induced Fluorescence Point Measurements.....	8
1.4 Instrumentation.....	9
1.4.1 Perkin Elmer NexION ICP-MS.....	9
1.5 Summary.....	10
1.6 References.....	11
2 Planar Laser Induced Fluorescence Images of Calcium and Barium Ion Beams.....	13
2.1 Introduction.....	13
2.2 Experimental.....	14
2.2.1 ICP-MS Modifications.....	15
2.2.2 Laser and Optics.....	17
2.2.3 Optimizing ICP-MS Performance.....	20
2.2.4 Solutions.....	21
2.2.5 Image Acquisition and Processing.....	21
2.3 Results and Discussion.....	24
2.3.1 Barium Ion Results.....	24
2.3.2 Calcium Ion Results.....	28
2.4 Conclusion.....	31
2.5 References.....	32
3 Beam Expansion in the Third Vacuum Stage.....	33

3.1	Introduction .....	33
3.2	Experimental .....	35
3.2.1	Instrumentation and Solutions .....	36
3.2.2	ICP-MS Modifications.....	36
3.2.3	Internal Optical Setup .....	38
3.2.4	Data Processing.....	40
3.3	Results and Discussion.....	41
3.3.1	Ba <sup>+</sup> Beam Expansion Profiles .....	41
3.3.2	Optical Crossover Volume.....	42
3.3.3	Deconvolution of Beam Divergence Angle .....	44
3.3.4	Instrument Drift and Hysteresis Effects.....	45
3.3.5	Evidence of Shock Structure.....	48
3.4	Conclusion.....	49
3.5	References .....	50
4	Future Work.....	51
4.1	Phase Two Calcium Study .....	51
4.2	New Hyperskimmer Design.....	52
4.3	LIF point measurements at the tip of the Hyperskimmer.....	52
4.4	References .....	53
5	Appendix A. Phase One Example Matlab Script .....	55
6	Appendix B. Phase Two Example Matlab Script.....	63

## LIST OF TABLES

Table 2.1.....	26
Table 2.2.....	30
Table 3.1.....	37

## LIST OF FIGURES

Figure 1.1.....	2
Figure 1.2.....	9
Figure 2.1.....	15
Figure 2.2.....	16
Figure 2.3.....	16
Figure 2.4.....	17
Figure 2.5.....	18
Figure 2.6.....	19
Figure 2.7.....	20
Figure 2.8.....	22
Figure 2.9.....	25
Figure 2.10.....	27
Figure 2.11.....	28
Figure 2.12.....	29
Figure 2.13.....	30
Figure 3.1.....	34
Figure 3.2.....	35
Figure 3.3.....	38
Figure 3.4.....	39
Figure 3.5.....	40
Figure 3.6.....	42
Figure 3.7.....	42
Figure 3.8.....	43
Figure 3.9.....	44
Figure 3.10.....	45
Figure 3.12.....	47
Figure 3.13.....	48
Figure 3.14.....	49



# 1 INTRODUCTION

## 1.1 ICP-MS Overview

The inductively coupled plasma mass spectrometer (ICP-MS) is an analytical instrument that was developed primarily for elemental analysis. An inductively coupled plasma atomizes and ionizes samples that are then separated based on their mass to charge ratio and finally counted electronically. ICP-MS is a desirable technique because of its low detection limits and high sensitivity. Since ICP-MS was commercially introduced in the 1980s it has been employed routinely in many fields.<sup>1</sup>

With an ability to detect most elements in the parts per trillion concentration range, ICP-MS is indispensable when it comes to high purity testing and ultra-trace analysis. ICP-MS is used in clinical settings to test for metal toxicity in blood or urine samples.<sup>2</sup> The Environmental Protection Agency employs ICP-MS to test heavy metal concentrations in drinking water.<sup>3</sup> ICP-MS is also used to detect contaminants in electronics,<sup>4</sup> pharmaceuticals,<sup>5</sup> and chemical reagents, all of which require a high level of purity to be effective. Other areas that employ ICP-MS include isotopic measurements, imaging, nanoparticle detection, metallomics, environmental monitoring, geochemistry, material sciences, semiconductor fabrication, nuclear technology, dietetics and biomedicine.<sup>6-10</sup>

### 1.1.1 ICP-MS Principle of operation

ICP-MS can analyze solid, liquid, or gas samples, but it most often deals with samples in aqueous solution. A schematic of a conventional ICP-MS is shown in Figure 1.1. Samples are pumped directly into the ICP-MS. They are first passed through a nebulizer, which generates a fine mist aerosol. Droplets containing the sample are carried downstream by argon gas. The sample is passed from the nebulizer tip, through a spray chamber, and into the torch.

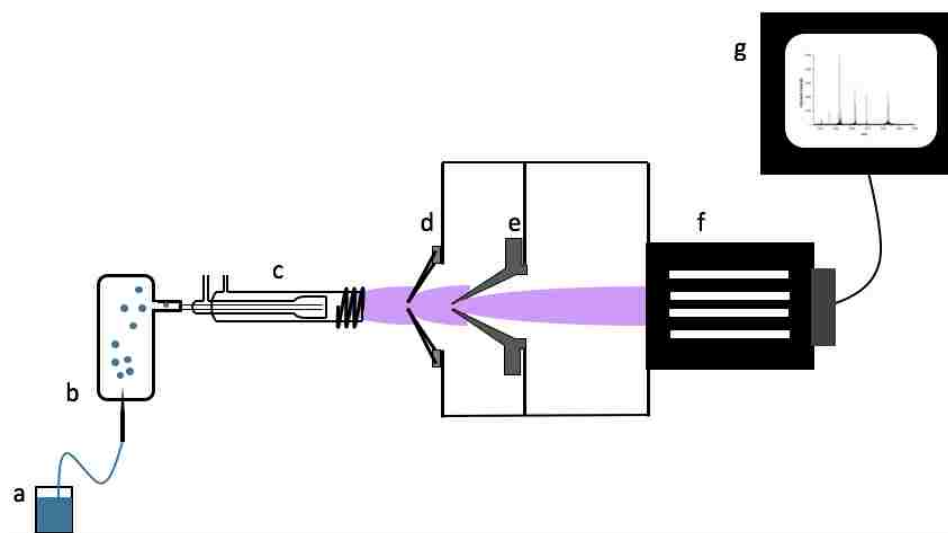


Figure 1.1 Schematic of a conventional ICP-MS. (a) sample. (b) Nebulizer and spray chamber. (c) The torch. (d) Sampling cone. (e) Skimmer cone. (f) Quadrupole mass analyzer. (g) Representative mass spectrum.

The torch is an assembly of three concentric quartz tubes designed to pass the sample aerosol as well as flow additional argon as a sheath gas. Around the torch is a three-turn copper wire. The copper wire conducts an alternating RF current, which generates an oscillating magnetic field. A Tesla coil spark initiates argon atom ionization. The electrons from the initial ionization are inductively heated as they are influenced by the oscillating magnetic field. Further collisions of electrons with other argon atoms generate a plasma of argon atoms, electrons, and

argon ions. A continuous supply of RF energy is used to sustain the plasma through inductive coupling.<sup>11</sup>

The ICP is a hard ionization source, operating at temperatures up to 8000 K. At these temperatures, the aerosol sample is readily ionized. First the solvent in each droplet is evaporated, exposing the sample. The sample molecules are then broken down into individual atoms and finally the atoms are ionized. In the plasma, there is enough thermal energy to remove one electron from almost every atom in the periodic table, but not enough thermal energy to remove more than one electron. However, only about 0.1% of argon atoms in the plasma are ionized. The degree of element specific ionization can be predicted using the Saha equation.<sup>12-13</sup>

Most often a quadrupole mass analyzer is used to detect which ions are present and to produce quantitative data on sample composition. Magnetic sector and time of flight mass analyzers can also be used. The mass analyzer operates at a low pressure of about  $10^{-6}$  torr. The plasma generated in the ICP begins at atmospheric pressure and must be pumped down through a series of vacuum stages until it matches the operating pressure of the mass analyzer.

Traditionally, the sampling interface between the ICP and the mass analyzer consists of two cones, the sampler cone and skimmer cone, and an orifice to the mass analyzer. First, ions pass through a sampler cone into the first vacuum stage, where the pressure is about 1 torr. In this vacuum stage, the ion beam expands rapidly until it mixes with the background gas, forming a barrel shock structure and Mach disk. The tip of the skimmer cone is placed inside the shock structures in a region called the zone of silence.<sup>14</sup> Only a small portion of the beam can then be extracted into the second vacuum stage through the skimmer cone. The second vacuum stage operates at about  $10^{-3}$  torr. Finally, the ions are focused through the orifice to the mass analyzer at a pressure of  $10^{-6}$  torr, and can be sorted and detected.

## 1.2 ICP-MS Limitations

Despite the technique's maturity, ICP-MS performance in some applications is still limited by poor ion transmission efficiency. Specifically, space charge effects, matrix effects, shock formation and other processes that govern ion beam extraction through the vacuum interface are not completely understood. Over the past three decades, numerous studies have been published that have slowly added to the overall understanding of how space charge affects ion transport efficiency,<sup>15-16</sup> how matrix effects are related to space charge,<sup>17</sup> and where ions are lost during the sampling and extraction processes.

### 1.2.1 Space Charge Effects

Samples in an ICP are atomized and ionized. The resulting plasma is composed of singly charged cations, electrons, as well as neutral species. While these species are present, the plasma remains quasi-neutral. Eventually the electrons are removed as the plasma is extracted into the vacuum system of mass spectrometer and shaped into a beam. The ion beam is now positively charged. Most studies indicate that charge separation happens somewhere inside the skimmer cone, although the exact position of charge separation is unknown.<sup>17-19</sup> The remaining cations experience Coulombic forces and mutually repel one another. This phenomenon is called space charge. Space charge leads to mass bias and matrix effects, and can limit the quantitative accuracy of ICP-MS by defocusing the ion beam.<sup>17</sup> Space charge and other matrix effects can sometimes be accounted for but are problematic when the sample composition is unknown.

Gilson et al.<sup>17</sup> found that some matrix effects are the direct result of space charge happening at the skimmer cone. His study shows that a mass discrimination takes place inside the skimmer cone and that changing the sample composition at the skimmer will change the

downstream intensity of a particular ion. Several other studies have also shown that heavier analyte ions are less affected by changes in sample composition than light analytes.<sup>18, 20-22</sup> Furthermore, Gilson et al. observed the addition of a heavy matrix element suppresses analyte signal more than the addition of a light matrix element. Allen et al.<sup>22</sup> used monodisperse dried microparticulate injection to investigate space charge and similarly found that the addition of lead ions influenced the profile of lithium ions. He observed more massive ions arriving at the detector slightly delayed with respect to the lighter ones, and that the first two extraction lenses also play a role in charge separation. Tanner et al.<sup>18</sup> used a computational model to predict the onset of space charge in the ion optics of instruments with cylindrical symmetry. His work showed that the mass bias can be extended to isotope ions of a single element. Tanner predicted that accelerating the ions downstream from the skimmer would minimize space charge effects but would also complicate detection at the mass analyzer.

A few studies have offered suggestions to minimize space charge effects at the skimmer cone. Turner et al.<sup>23</sup> used an acceleration cone biased at  $-2000$  V behind the skimmer, and found a reduction in matrix effects. However, they were not eliminated completely. Praphairaksit et al.<sup>15</sup> showed that an electron source behind the skimmer could reduce space charge effects by adding electrons back to the ion beam after the charge separation event had occurred. The use of this filament also improved ion transmission efficiency. Tanner et al.<sup>24</sup> took a different approach to minimize Coulombic repulsion in the ion beam by extracting the beam through a three aperture interface. His results showed a decrease in mass discrimination and a narrow range of mass-based ion kinetic energies. Tanner proposed that space charge arises in the ion optics of the ICP-MS and can be minimized by reducing the ion current through a third aperture.

### 1.2.2 Sampling Efficiency

ICP-MS operating parameters and instrument design also influence ion transmission efficiency. Soon after the commercial introduction of ICP-MS, Vaughan et al.<sup>25</sup> investigated the effects ion lens voltage, plasma power, sampling depth, and nebulizer flow rate on the analyte ion signal. Macedone et al.<sup>26</sup> also studied the effects of nebulizer flow rates on ion transport efficiency, as well as the effects of sample composition, RF forward power, and torch shield configuration. All of these parameters were found to play a role in ion transmission and need to be optimized for ideal performance. Taylor et al.<sup>27</sup> observed that the geometry of the skimmer cone affects the strength of the shock structure and secondary expansion that originates inside the tip of the skimmer cone. Taylor also found that increasing the skimmer orifice diameter allows more ions into the second vacuum stage.

### 1.3 Background

Space charge effects and ion transmission losses persist despite numerous studies investigating these two main limitations of ICP-MS. Understanding space charge effects and ion transmission losses at the fundamental level has proven to be challenging. Commercially-available software cannot readily model the intense ion beam generated by the ICP. Experimental data are necessary to supplement and improve computer models, but experimental characterization of the ion beam is difficult. There is limited space within the first and second vacuum stages of ICP-MS, making it nearly impossible to probe the ion beam without affecting its overall behavior. A non-invasive experimental technique is needed to probe ICP-MS and provide insight to the fundamental causes of space charge and ion losses.

### 1.3.1 Planar Laser Induced Fluorescence Second Vacuum Stage Studies

Recently, two studies demonstrated the ability to measure cross sections of Ca and Ba ion beams in an ICP-mass spectrometer just a few millimeters upstream from the entrance to the mass analyzer in a working commercial instrument using planar laser-induced fluorescence (PLIF).<sup>16, 28</sup> The advantage of PLIF over previously-used beam profiling approaches is that it is element-specific and non-invasive. The measurements exploited the unique ion reflector in the Varian 820 ICP-MS that introduces a 90-degree bend in the ion beam. The Ca study<sup>16</sup> demonstrated that the shapes and sizes of the ion beams were reasonably approximated by Simion simulations, and that the effects of moderate concentrations of concomitant sample species on beam profiles were relatively small. The notable exception was the effect of added Pb in the sample on the behavior of the Ca ion beam. The addition of 1.5 mM Pb to the sample solution shifted the Ca ion beam laterally far enough to cause an order-of-magnitude drop in the Ca ion signal.

Additionally, as was observed in the Ca study, the presence of lead in the matrix caused a position shift of the Ba beam approximately 1 mm to the right, with respect to the entrance of the mass analyzer.<sup>28</sup> The experimental data confirmed simulation data that the ions follow a mass dependent path from the skimmer cone, through the turn in the ion reflector, and into the mass analyzer. The result is that under compromise focusing conditions for a wide mass range, the heavier masses enter the mass analyzer on the left side of the entrance aperture and the lighter masses on the right. It was can concluded from these studies that the lateral shifts in the ion beam are caused by Coulombic repulsion between the spatially separated Pb ion beam and either the Ca or Ba analyte beam. Once more ion beam profiles were obtained noninvasively and used to confirm simulation data.

### 1.3.2 Laser Induced Fluorescence Point Measurements

The work presented in this thesis was performed in two phases. The first phase expands the work described in the previous section by using PLIF to characterize the ion beam in a Perkin Elmer NexION ICP-MS. The second phase characterizes beam expansion into the third vacuum stage of the NexION.

Second phase measurements were taken at the base of the hyperskimmer cone, which is the third cone in the instrument's unique vacuum interface. In this region, instrument performance was compared to ideal skimming. Phase two also used laser induced fluorescence, LIF, but point measurements were recorded instead of planar images.

A similar experiment was performed previously. Radicic et al. used LIF point measurements to characterize the first vacuum stage supersonic expansion in a mockup instrument.<sup>29</sup> Radicic et al. monitored neutral argon atoms downstream from the tip of the sampler cone. They found the first stage expansion was consistent with detailed fluid dynamic theory but had some significant differences from the simplified theory, which could lead to a bad skimmer cone position relative to the shock structures formed in the first vacuum stage. The work in this thesis uses a similar setup as Radicic et al. to monitor  $\text{Ba}^+$  ion velocities and trajectories as the ion beam is extracted into the last vacuum stage before the mass analyzer.



## 1.4 Instrumentation

### 1.4.1 Perkin Elmer NexION ICP-MS

The entirety of this project was completed on a Perkin Elmer NexION ICP-MS 300S. The internal layout of the NexION can be seen in Figure 1.2, where the green line marks the path traveled by the ions.

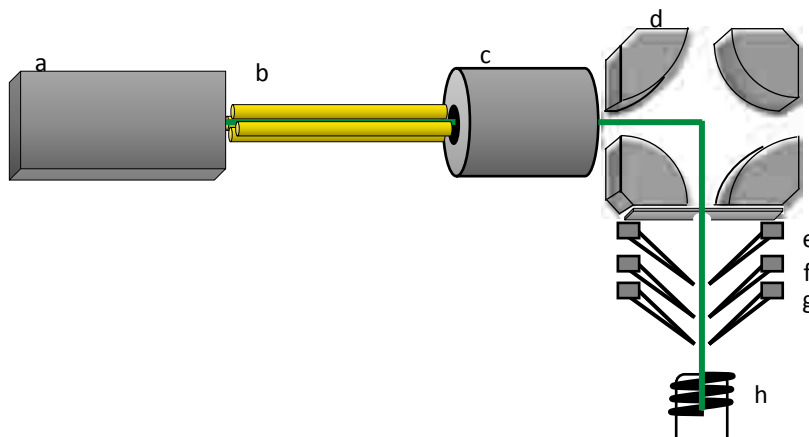


Figure 1.2 Internal components and ion path of the NexION ICP-MS. The instrument components are a) detector, b) quadrupole mass filter, c) universal cell, d) quadrupole ion deflector, e) hyperskimmer cone, f) skimmer cone, g) sampler cone, h) torch. The green trace represents the path of the ions. Components are not drawn to scale.

The NexION differs from traditional ICP-MS configurations. First the NexION uses a three-cone interface. The third cone is called a hyperskimmer cone and is mounted directly behind the skimmer cone. Second the NexION differs from other ICP-MS systems in that no extraction lenses are used behind the sampling interface to shape the ion beam in the second vacuum stage. Finally, and perhaps the most significant difference between the NexION and traditional ICP-MS systems is that the NexION uses a quadrupole ion deflector, QID, to bend the ion beam 90 degrees. In other words, the axis down the center of the cone interface is orthogonal

to the center axis through orifice of the mass analyzer. This is a similar geometry to that of the Varian 820 model. The idea with this design feature is to decrease background signal by allowing neutral particles to continue along their linear trajectory and manipulate only the positively charged ions 90 degrees and into the mass analyzer.

The 90-degree geometry is what makes fluorescent imaging possible in a working instrument. We have taken advantage of this design and modified components of the instrument housing allowing us to introduce laser radiation and couple fluorescence collection optics to the system without affecting instrument performance.

Further, we probed the region behind the hyperskimmer cone using a second set of modifications and fiber optics to take point measurements. The modifications required for both experimental designs will be described in chapters 2 and 3 respectively.

## 1.5 Summary

Space charge effects and ion transmission losses limit the performance of ICP-MS. Many studies have been conducted to understand space charge and ion transport efficiency but they continue to be the main limitations of ICP-MS. Experimental data is needed to support simulation data. PLIF is a noninvasive technique that takes advantage of the NexION ICP-MS geometry and produces images of the ion beam in a working instrument. Further, the exact position of charge separation is unclear, but is thought to occur inside the tip of the skimmer cone. This poses an interesting question for the NexION which utilizes a three-cone interface. Point measurements are taken at the base of the hyperskimmer cone and the effect of this interface on ideal skimming will be discussed.

## 1.6 References

1. Houk, R. S., *Acc. Chem. Res.* 1994, 27, 333-339.
2. Goulle, J. P.; Mahieu, L.; Castermant, J.; Neveu, N.; Bonneau, L.; Laine, G.; Bouige, D.; Lacroix, C., *Forensic Science International* 2005, 153, 39-44.
3. Wolf, R. E.; Grosser, Z. A., *At. Spectrosc.* 1997, 18, 145-151.
4. Pedreira, W. R.; Queiroz, C. A.; Abrao, A.; Rocha, S. M.; de Vasconcellos, M. E.; Boaventura, G. R.; Pimentel, M. M., *J. Alloys Compd.* 2006, 418, 247-250.
5. Rao, R. N.; Talluri, M., *J. Pharm. Biomed. Anal.* 2007, 43, 1-13.
6. Koppenaal, D. W., *Anal. Chem.* 1992, 64, R320-R342.
7. Degueldre, C.; Favarger, P. Y., *Colloids and Surfaces a-Physicochemical and Engineering Aspects* 2003, 217, 137-142.
8. Szpunar, J., *Analyst* 2005, 130, 442-465.
9. Yang, L., *Mass Spectrom. Rev.* 2009, 28, 990-1011.
10. Becker, J. S.; Matusch, A.; Becker, J. S.; Wu, B.; Palm, C.; Becker, A. J.; Salber, D., *Int. J. Mass spectrom.* 2011, 307, 3-15.
11. Boss, C. B.; Fredeen, K. J., General Characteristics of ICP-OES. In *Concepts, Instrumentation, and Techniques in Inductively Coupled Plasma Optical Emission Spectrometry*, 2 ed.; The Perkin-Elmer Corporation: Norwalk, CT, 1999.
12. Houk, R. S., *Anal. Chem.* 1986, 58, A97-&.
13. Crain, J. S.; Smith, F. G.; Houk, R. S., *Spectrochim. Acta, Part B* 1990, 45, 249-259.
14. Douglas, D. J.; French, J. B., *J. Anal. At. Spectrom.* 1988, 3, 743-747.
15. Praphairaksit, N.; Houk, R. S., *Anal. Chem.* 2000, 72, 2356-2361.
16. Edmund, A. J.; Bergeson, S. D.; Lyon, M.; Taylor, N.; Kalinitchenko, I.; Farnsworth, P. B., *Spectrochim. Acta, Part B* 2012, 76, 109-118.
17. Gillson, G. R.; Douglas, D. J.; Fulford, J. E.; Halligan, K. W.; Tanner, S. D., *Anal. Chem.* 1988, 60, 1472-1474.
18. Tanner, S. D., *Spectrochim. Acta, Part B* 1992, 47, 809-823.
19. Niu, H.; Houk, R. S., *Spectrochim. Acta, Part B* 1996, 51, 779-815.
20. Tan, S. H.; Horlick, G., *J. Anal. At. Spectrom.* 1987, 2, 745-763.
21. Burgoyne, T. W.; Hieftje, G. M.; Hites, R. A., *Anal. Chem.* 1997, 69, 485-489.
22. Allen, L. A.; Leach, J. J.; Houk, R. S., *Anal. Chem.* 1997, 69, 2384-2391.
23. Turner, P. J., Some Observations on Mass Bias Effects Occurring in ICP-MS Systems. In *Applications of Plasma Source Mass Spectrometry*, Holland, G.; Eaton, A. N., Eds. Royal Society of Chemistry: Cambridge, U.K., 1991; pp 71-78.
24. Tanner, S. D.; Cousins, L. M.; Douglas, D. J., *Appl. Spectrosc.* 1994, 48, 1367-1372.
25. Vaughan, M. A.; Horlick, G.; Tan, S. H., *J. Anal. At. Spectrom.* 1987, 2, 765-772.
26. Macedone, J. H.; Gammon, D. J.; Farnsworth, P. B., *Spectrochim. Acta, Part B* 2001, 56, 1687-1695.
27. Taylor, N.; Farnsworth, P. B., *Spectrochim. Acta, Part B* 2012, 69, 2-8.
28. Larsen, J. J.; Edmund, A. J.; Farnsworth, P. B., *Spectrochim. Acta, Part B* 2016, 125, 61-65.
29. Radicic, W. N.; Olsen, J. B.; Nielson, R. V.; Macedone, J. H.; Farnsworth, P. B., *Spectrochim. Acta, Part B* 2006, 61, 686-695.



## 2 PLANAR LASER INDUCED FLUORESCENCE IMAGES OF CALCIUM AND BARIUM ION BEAMS

### 2.1 Introduction

The experiments that make up phase one of my research project are discussed in this chapter. Planar laser induced fluorescence (PLIF) images were taken of the  $\text{Ca}^+$  and  $\text{Ba}^+$  ion beams upstream of the entrance to the mass spectrometer. Specifically, the ion beams were imaged 0.75 mm in front of the entrance to a collision/reaction cell called the universal cell, and directly after the beams exit the quadrupole ion deflector (QID), refer to Figure 1.2. The images described in this chapter are valuable because they allow a direct comparison between the actual performance of the ion optics and the performance predicted by simulations. The PLIF images primarily show the spatial distribution of ion densities within the beam. The images also give a qualitative picture of beam convergence or divergence.

The beam convergence is best seen in a series of images that will be referred to as the velocity distribution images. Not all of the ions in the ion beam travel in parallel paths at the same speed, although that kind of beam homogeneity would be ideal. As the beam interacts with a stationary plane of laser light, the ions respond to different frequencies of light based on their velocity. Due to this Doppler Effect, only a portion of ion density is excited at any given incident wavelength. Using this to our advantage, the incident laser wavelength was scanned over the Doppler-broadened transition and a series of images was generated for each analyte ion. The

nature of this measurement showed how well the beam was collimated based on the wavelength range necessary to fully image the beam. Additionally, we calculated the velocity component of ion motion parallel to the plane of laser radiation for each image in the distribution. In other words, we calculated the velocity component of the ion beam perpendicular to the overall direction of travel. This gives a qualitative picture of how fast the beam was converging or diverging.

The spatial distribution of ion density is best seen in a summation of the velocity distribution images. The composite image shows a cross section of what the total ion beam looks like in the plane of laser radiation. The spatial distribution in combination with the velocity distribution indicate instrument performance by showing the ability of the ion optics to tightly focus ions and deliver them to the mass analyzer.

## 2.2 Experimental

The basic experimental design for the PLIF experiments has been previously described,<sup>1</sup> and an overview of the design is shown in Figure 2.1. Briefly, frequency doubled light from a tunable CW (continuous wave) titanium-sapphire laser served as the excitation source. Active feedback electronics tuned and locked the laser and frequency doubling cavity to a desired excitation wavelength. A plane of laser radiation was created by focusing the frequency doubled light through two cylindrical lenses. The radiation plane was introduced to the NexION, in the third vacuum stage, and was focused between the exit of the quadrupole deflector and the entrance to the mass analyzer. A CCD captured the fluorescence. A series of exposures were acquired at 0.001nm intervals over the Doppler width of the fluorescence excitation profile for

the analyte ion. The images were recorded as a function of excitation wavelength. Finally, the composite ion beam images were generated from the normalized sum of velocity distribution.

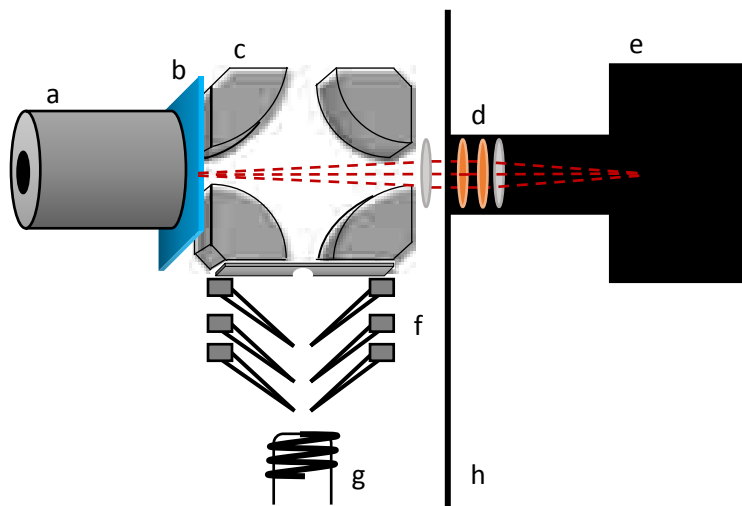


Figure 2.1 Experimental setup overview. (a) the universal cell, (b) the plane of laser radiation, (c) QID, (d) collection optics with focusing lenses in grey and filters in orange, (e) CCD, (f) three cone vacuum interface, (g) torch, (h) outer wall of vacuum chamber. A plane of laser radiation is focused between the QID and universal cell. The fluorescence is captured by a CCD on the outside of the vacuum chamber.

### 2.2.1 ICP-MS Modifications

Several modifications were made to the instrument to allow optical access without affecting instrument performance. Laser radiation was introduced to the third vacuum stage through a modified lid over the vacuum chamber, shown in Figure 2.2. The plane of laser radiation had to be perfectly vertical and centered above the gap between the QID and the universal cell. Starting from a blank lid piece, two RF feedthroughs and two fused silica windows were built into the lid. The RF feedthroughs were moved back from the original design of the chamber lid to allow room for the windows. This also meant that the circuit board, heat sink, and cooling fan had to be repositioned, as can be seen in Figure 2.3. The purpose of the first window was to help us see inside the chamber to align and focus the laser beam. The laser light

passed through the second window, which was centered directly above the QID- universal cell gap. The second window was attached underneath the chamber lid. The lid above the second window was threaded to be compatible with 1- inch Thorlabs (Newton, New Jersey) lens tubes allowing us to mount our beam shaping optics directly to the lid.

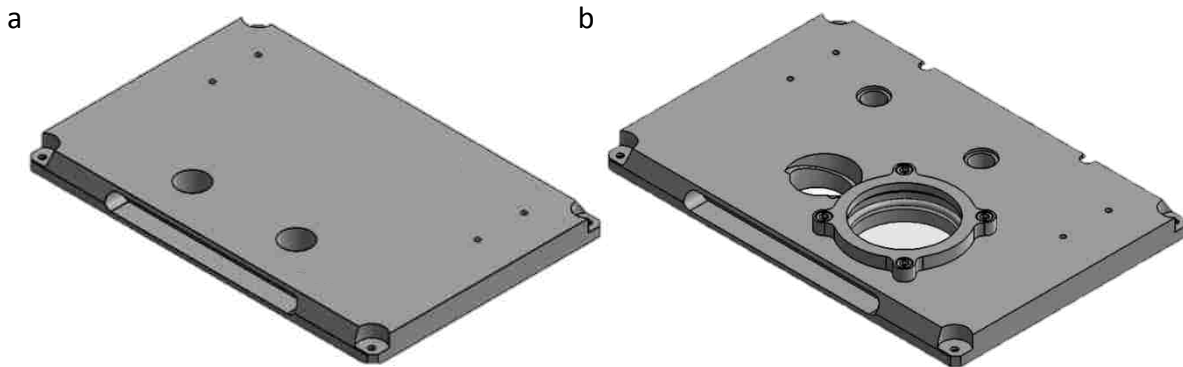


Figure 2.2 Modified vacuum chamber lid. Frame (a) shows the original lid design with the RF feedthroughs located at the front edge of the plate and 4 threaded holes at the back of the plate to attach the circuit board, heat sink, and cooling fan directly to the lid. Frame (b) shows the modified lid. The RF feedthroughs have been moved to the back. In front the window on the left is compatible with Thorlabs tubes. The window on the right is for aligning the plane of laser light. Note that an adapter piece, not shown, was attached to the modified lid that coupled to the circuit board, heat sink, and cooling fan.

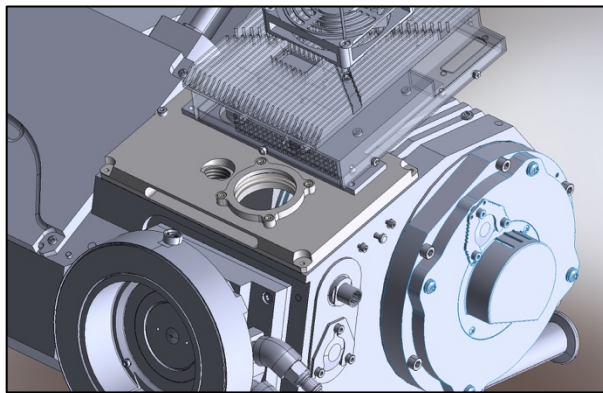


Figure 2.3 Modified lid attached to the NexION with the circuit board, heat sink, and cooling fan in place.

The other important modification was replacing a side vacuum port with a fused silica window. This allowed the collection optics to capture the fluorescence. The port that was modified can be seen in Figure 2.3, but a close up of the port and the new window adaptor piece



is shown in Figure 2.4. The fluorescence was focused through this port and onto a CCD mounted directly outside the instrument.

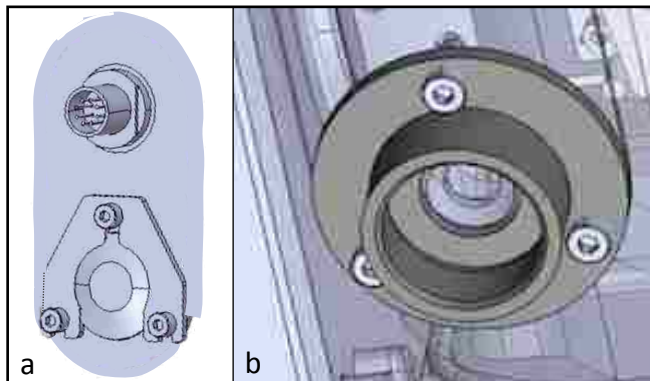


Figure 2.4 Modified vacuum port on the side of the NexION. Frame (a) shows the original port (port can also be seen in Figure 2.2). Frame (b) shows the adaptor piece used to mount a glass window directly to the NexION, thus allowing the fluorescence to be captured by a CCD outside of the instrument.

### 2.2.2 Laser and Optics

A tunable, CW titanium-sapphire laser (SolsTis, M Squared Lasers, Glasgow, Scotland) was used as the fluorescence excitation source. We built two bowtie cavities, each with a wavelength specific, lithium triborate crystal to frequency double the laser light. The laser layout is presented schematically in Figure 2.5. An electro-optical modulator (EOM) and photodiode (PD) were used to lock the laser to the cavity to the desired output wavelength using the Pound-Drever-Hall method.<sup>2</sup> For this phase of the experiments the frequency-doubled output of the cavity was tuned by manual adjustment of a voltage applied to a piezo-electric stack behind one mirror in the doubling cavity. The error signal from the lock box was applied to the cavity of the pump laser, forcing the pump laser to track the frequency-doubled cavity. The pump laser wavelength was monitored using a precision wavemeter (Angstrom WS/6, High Finesse, Tübingen, Germany).

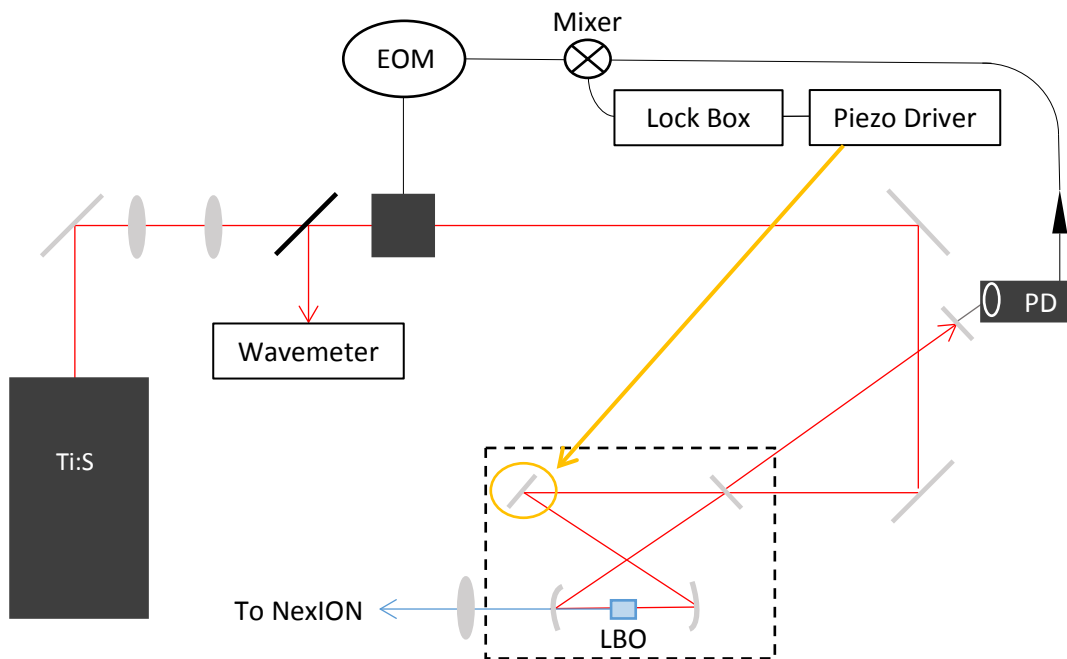


Figure 2.5 Frequency doubling cavity and active feedback control. Signals from the EOM and PD were mixed and the resulting error signal was fed back to the laser to lock to a wavelength. The voltage output of the piezo-electric driver was manually adjusted to tune the wavelength over a small range. Frequency doubling occurred in an LBO crystal cut specifically for the Ba or Ca transition of interest.

A plane of laser radiation was then created by focusing the frequency doubled light through two cylindrical lenses. The cylindrical lenses were mounted to the lid of the NexION ICP-MS above the third vacuum stage, allowing the plane of laser radiation to be focused between the exit of the quadrupole deflector and the entrance to the mass analyzer. The arrangement is illustrated in Figure 2.6.

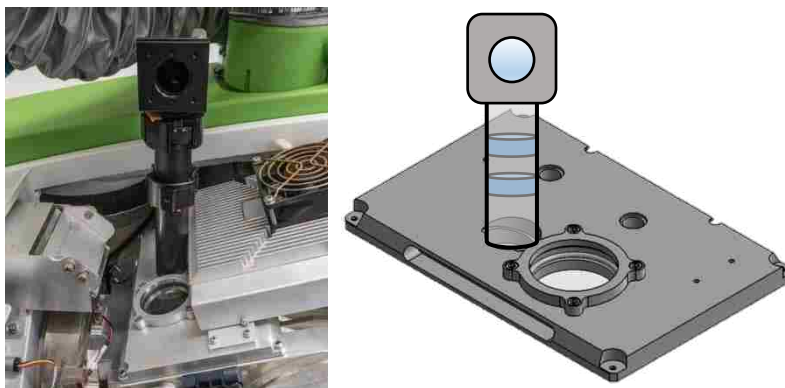


Figure 2.6 Optics mounted to lid of NexION ICP-MS. A pair of cylindrical lenses shaped the laser beam into a plane of radiation and focused the plane in the gap between the universal cell and the QID.

The collection optics were positioned on the opposite side of the QID as shown in Figure 2.1. A CCD captured the fluorescence and the images were recorded as a function of excitation wavelength. It was necessary to mount the first lens of the collection optics inside the instrument to ensure that the images were properly magnified and to maximize the overall efficiency of the collection optics. To mount the first lens inside the instrument we designed a mount that attached to the QID. This lens mount also needed to easily move in and out of place so a focusing target could be placed inside the vacuum chamber through the open side port. The pivot lens mount was made of non-conducting material and did not affect instrument performance. The mount is depicted in Figure 2.6. The achromatic lens in the pivot mount collimated the light and was the only component of the collection optics located inside the instrument. The collimated light passed through the window mounted to the vacuum port, and then passed through two filters, a long pass filter and a band pass filter. Finally, it was focused onto the CCD with a second achromatic lens. Both the filters and the second lens were mounted in Thorlabs one-inch tubes that were threaded on to the face of the CCD.

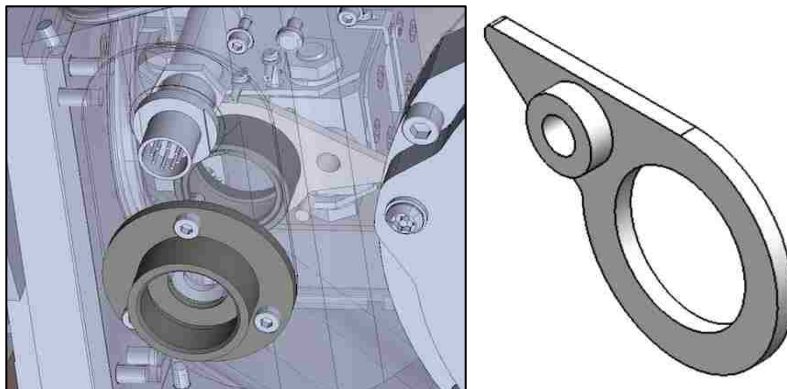


Figure 2.7 Collection optics internal lens mount. The lens mount is designed to pivot in and out of position when needed, and is attached directly to the QID as shown in the left frame.

### 2.2.3 Optimizing ICP-MS Performance

Overall NexION performance was monitored and optimized using the NexION tuning solution and optimization programs built into the NexION software. The instrument had to pass all of the performance requirements before any data were collected. The performance was checked routinely. The automated tests included the torch position, mass calibration, nebulizer gas flow rate, autolens voltages, and a daily performance check. The ions monitored in the daily performance check included Be, Mg, In, U, CeO/Ce, Ce<sup>2+</sup>/Ce, and the background.

Once optimal performance was achieved, the settings were saved. The final step in optimizing instrument performance was tuning the QID to the analyte mass. In a typical application, the QID is dynamic, meaning that the voltages applied to the QID change depending on the mass selected to pass through to the universal cell. In this application, a single mass was monitored continually. The QID was set to a static voltage and the deflector voltage was manually varied in small steps until the signal for the isotope of interest was maximized. In order to maximize the fluorescence, sample solutions were 1000 times more concentrated than what is typically monitored. Therefore, minor isotopes of Ca and Ba, Ca-43 and Ba-130 respectively,

were monitored to avoid damaging the detector. Additionally, the voltage applied to the electron multiplier was dropped until the signal for the analyte was reading less than 200,000 counts  $s^{-1}$  at the mass spectrometer.

#### 2.2.4 Solutions

Ca and Ba analyte solutions were made from Ca nitrate and Ba nitrate (J.T. Baker Chemical Co., Phillipsburg, NJ) dissolved in trace metal grade nitric acid (Thermo Fisher Scientific Inc., Waltham, MA) and diluted to 2% nitric acid with 18 M $\Omega$  deionized water (Millipore, Billerica, MA). The final concentrations of the solutions were 1.25 mM Ca and Ba respectively (50 mg  $L^{-1}$  Ca and 171 mg  $L^{-1}$  Ba respectively).

Instrument performance was evaluated using a Perkin Elmer tune solution (Waltham, MA). The solution contained 10 ppb (10  $\mu g L^{-1}$ ) of the following ions in 1% nitric acid: Be, Ce, Fe, In, Li, Mg, Pb, and U. Dilute nitric acid, 1%, was used as wash solution between all experiments and during instrument warm-up.

#### 2.2.5 Image Acquisition and Processing

This section describes all the elements incorporated into a Matlab script that was used to normalize and process the PLIF images. A representative example of the Matlab script has been included in Appendix A.

The first two images taken were of the orifice to the universal cell without the laser or the plasma on. This was done using a flashlamp and a 20 second CCD exposure. The first image was of a focusing target mounted inside the universal cell orifice. The focusing target was specially designed to help us align our plane of laser radiation to the center of the gap between the QID

and the universal cell and focus the CCD to the region of interest. The target is shown in Figure 2.8. The second image was taken of just the orifice for later superposition with the composite ion beam. The superposition of these images indicated the spatial position of the beam relative to the entrance to the universal cell and roughly showed how many ions would pass through that interface.

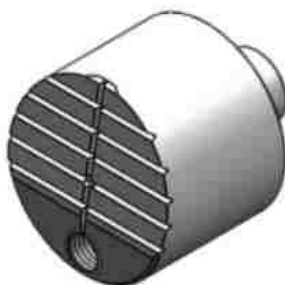


Figure 2.8 Focusing target. The target was mounted in the entrance to the universal cell. The front face is angled and acts as a laser guide. The hole at the bottom is so the target can be attached to a mounting rod in order to place the target without removing the QID.

Next the ICP was turned on. The instrument warmed up, and the cones were conditioned. Conditioning the cones entails running the instrument with the sample solution for a certain amount of time, typically one hour, to minimize changes in sample signal as instrument components become dirty. Then 1% nitric acid wash was pumped into the ICP. The laser was turned on and a blank image was taken using the same exposure time that the data set would use. The exposure was three minutes for Ca and two minutes for Ba. Finally, the analyte solution was pumped into the ICP, and a series of exposures was taken as the laser wavelength was tuned. For each image, several other pieces of information were recorded: laser power, mass counts, frequency, and wavelength. The mass counts were automatically saved to a file, but the other values were recorded manually.

Every image in a data set was normalized for differences in laser power. This was done automatically in Matlab by selecting a region of pixels in each image that corresponds to a place on the universal cell from which light was being scattered. The scattered light and the fluorescence signal were proportional to the laser power. The signals from each pixel in the selected scatter region were averaged. A ratio of the averaged scattered light for each image and the averaged scattered light to a selected standard image was used to normalize all the images and the blank to the same effective laser power. The laser power was also manually recorded with a power meter to double check this correction factor.

Every image in the data set also had to be normalized for the mass counts at the detector. Over time the sampler, skimmer, and hyperskimmer cones became clogged, and fewer ions could pass through the vacuum interface. To minimize changes in the mass count signal, the cones were conditioned for one hour before taking data. When the cones were unconditioned the mass counts dropped by a factor of 3 over the course of a data set acquisition. When the cones are conditioned this factor drops to about 1.3 for  $\text{Ba}^+$  and 1.7 for  $\text{Ca}^+$ . The mass counts were recorded for the duration of the experiment and time stamps were also taken for each image. The images were lined up with corresponding counts from the mass counts file. All the mass counts for a given exposure were averaged together. Ratios of average mass counts for the image taken in the middle of the data set to the average mass counts for each individual image were used to normalize all the images in a data set.

For the final image acquired as part of a data set, all the lights were turned off. The laser and plasma were also turned off and a black cloth was used to cover the CCD. A five second exposure was taken to record the CCD dark current. The dark current had to be subtracted from every image, including the blank, to obtain a correct normalization factor.

Once processed, the images could be viewed individually to isolate components of the beam with a specific velocity in the plane of the laser radiation, or combined to form a composite image. The most accurate composite was obtained by simply summing the processed images. However, for Ca, the S/N was poor in such a sum, and an alternative image was created by selecting for each pixel in the composite the most intense corresponding pixel from the set of individual images. This latter approach distorted the concentration distribution in the image, but better defined the boundaries of the ion beam.

## 2.3 Results and Discussion

### 2.3.1 Barium Ion Results

The Ba velocity distribution is shown in Figure 2.9. Each frame shows a packet of ions with the same velocity component perpendicular to the overall ion beam motion, i.e. in the plane of the page. The arrow on each frame points in the direction the ion packets are moving. The arrow length is proportional to the magnitude of the ion velocity. Ion densities are set to the same color scale, which represents the normalized CCD counts. The corresponding fundamental vacuum wavelength is listed on each image in nm.



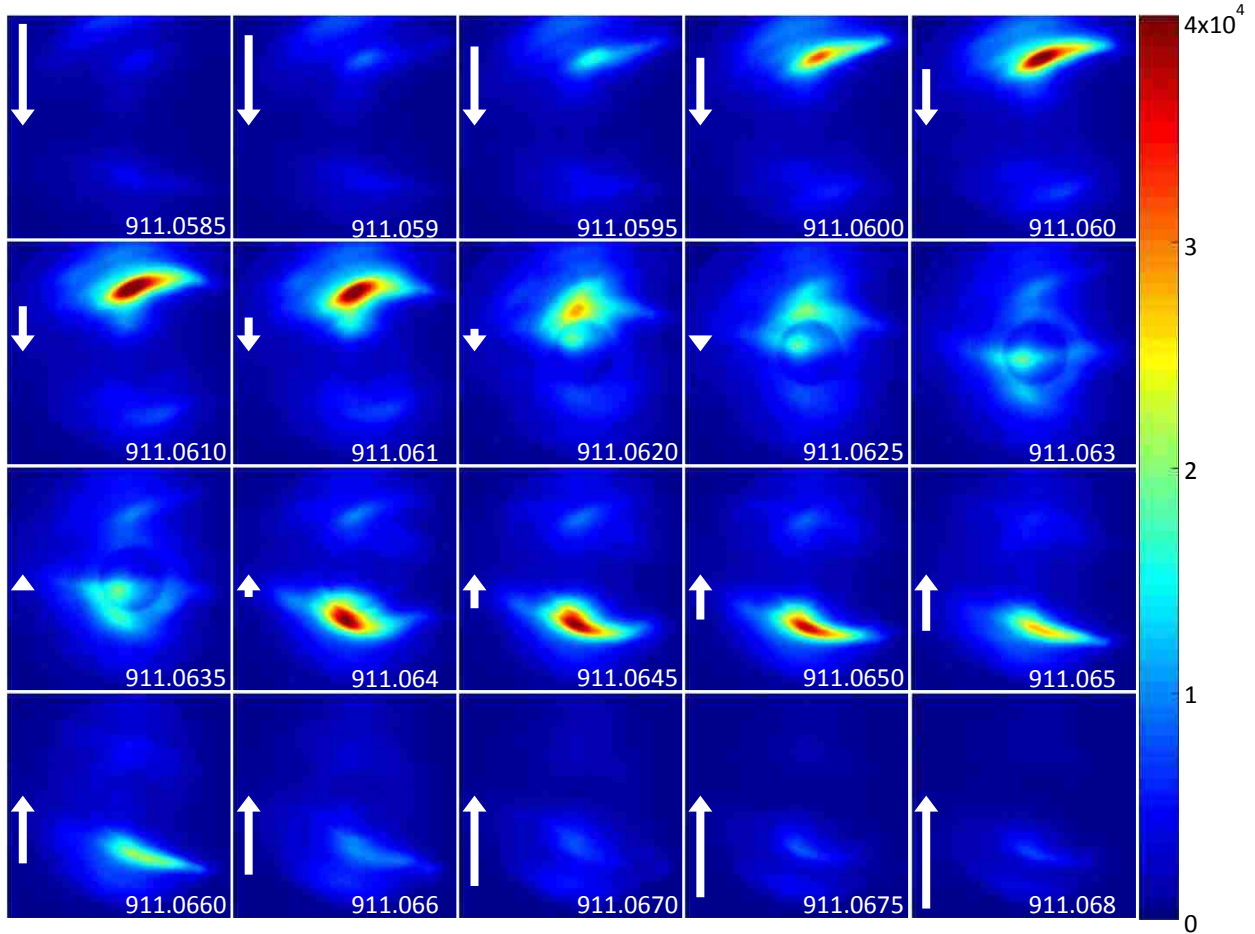


Figure 2.9 Ba velocity distribution. Arrow Length indicates the magnitude of ion velocity in the direction the arrow is pointing. All images are set to the same scale, with the fundamental vacuum wavelength listed for each image in nm. Color scale represents normalized counts at the CCD.

The velocities for each frame were calculated from frequency shifts,  $\Delta\nu$ , using the following equation

$$V = \frac{\lambda_{max}\Delta\nu}{\cos\theta} \quad (2-1)$$

where  $V$  is the velocity of the ions,  $\lambda_{max}$  is the excitation wavelength for a motionless population relative to the laser plane, and  $\theta$  is the angle of the incident light relative to the motion of the ion beam. The velocities are listed in table 2.1.

Table 2.1 Ba<sup>+</sup> velocities. Wavelengths are vacuum, and direction of travel is either up or down in the plane of the page, parallel to the laser radiation.

Wavelength (nm)	Velocity (m s <sup>-1</sup> )	Direction of travel
911.0679	1639.9223	u
911.0674	1457.7078	u
911.0668	1275.4935	u
911.0665	1184.3865	u
911.0660	1002.1726	u
911.0654	819.9589	u
911.0649	637.7454	u
911.0643	455.5322	u
911.0640	364.4256	u
911.0635	182.2127	u
911.0629	0.0000	n/a
911.0627	91.1063	d
911.0621	295.4050	d
911.0616	455.3184	d
911.0610	615.2316	d
911.0604	775.1447	d
911.0602	935.0578	d
911.0596	1094.9705	d
911.0591	1254.8830	d
911.0585	1414.7953	d

The composite Ba ion beam image is given in Figure 2.10. The composite image is a sum of the normalized individual images, and represents all the Ba ions present in the beam. This image shows two distinct lobes of ion density. Using the velocities calculated from the distribution images we know that these two lobes are rapidly converging as they approach the entrance to the universal cell.

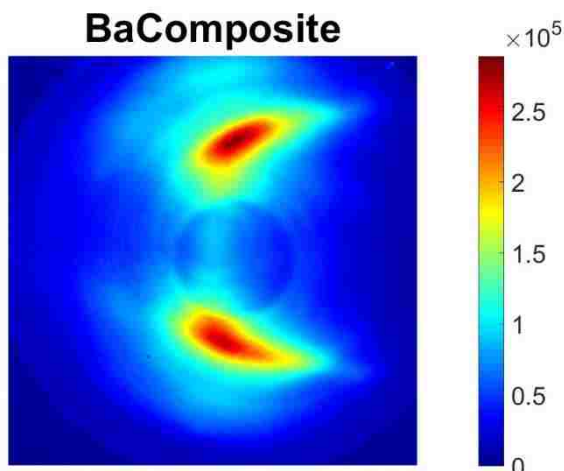


Figure 2.10 Total Ba ion beam. Image is a cross section of the Ba ion beam 0.75 mm in front of the entrance to the universal cell. Two distinct lobes of ion density are rapidly converging as they approach the cell entrance. Color scale represents normalized counts at the CCD.

Only a small portion of ion density is actually located in the center of the ion beam. By superimposing the total ion beam image and the image of the entrance to the universal cell, see Figure 2.11, we can see how much of the beam is centered on the aperture it is supposed to travel through. Because these images were recorded under conditions that optimized signal through the entire instrument, we infer that the majority of the ions have converged on the aperture by the time that they reach it. Because the velocities of the ions along the main axis of the mass analyzer (perpendicular to the page) are not known, the angles of convergence cannot be determined experimentally.

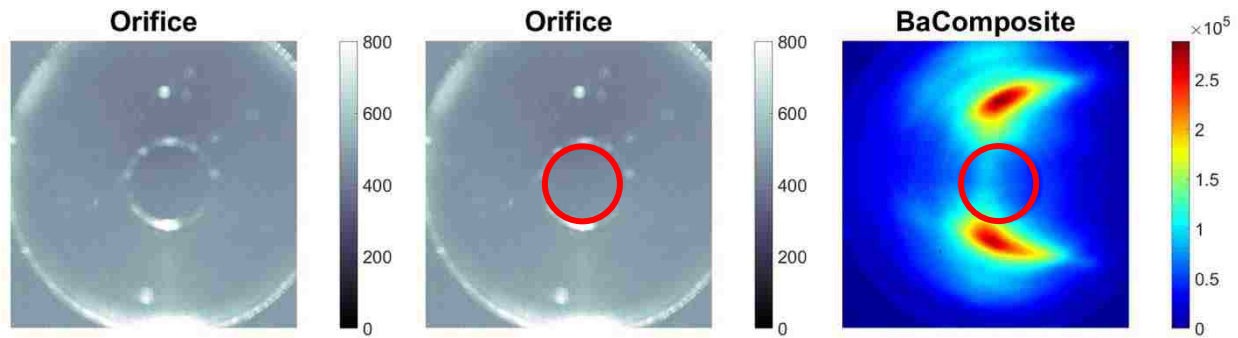


Figure 2.11 Superposition of universal cell entrance to the Ba ion beam. On the left is the image of universal cell entrance taken by the CCD. The middle image shows a cartoon superimposed on the orifice representing where the aperture is located. The cartoon is again shown in the frame on the right. Almost no ion density is located in the center of the aperture. Color scale represents normalized counts at the CCD.

### 2.3.2 Calcium Ion Results

The Ca velocity distribution is shown in Figure 2.12. Please note that the color scales for Ca and Ba are not the same. Again, the arrow length shows the velocity components of the ion packets parallel to the laser plane. Ca velocities can be seen in table 2.2. The ions that fluoresce at 786.9565 nm are not moving up or down but are traveling on-axis into the orifice. Because the fluorescence is much weaker for Ca than Ba, the composite image is difficult to distinguish from the total background; this can be seen in Figure 2.13. We processed the total ion beam using the second method described in section 2.2.5 to map out the region where any ions were present. However, this method requires a loss of spatial density information and makes the whole ion beam appear to have the same intensity. We need both versions of the total ion beam to understand what is going on.

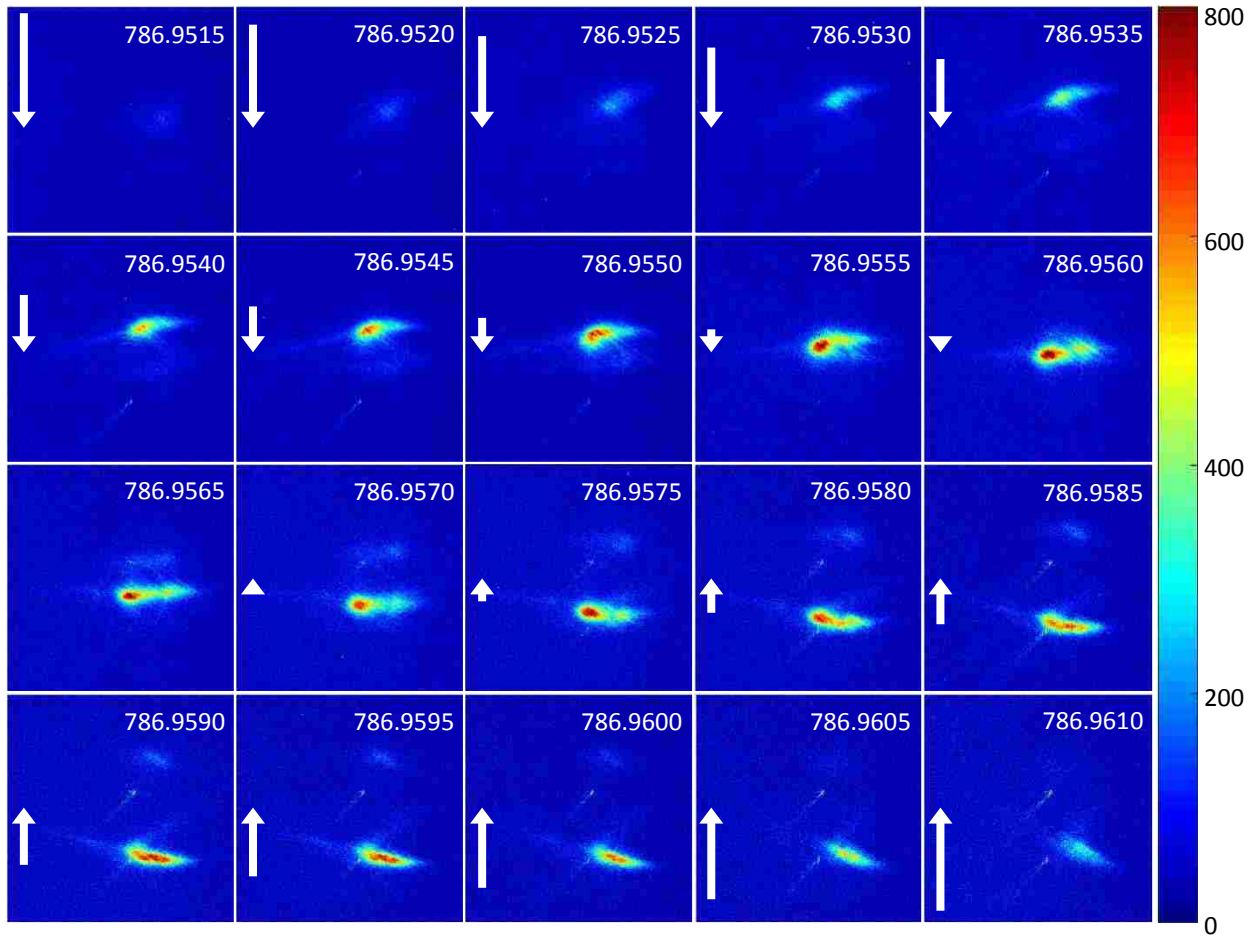


Figure 2.12 Ca velocity distribution. Arrow Length indicates the magnitude of ion velocity in the direction the arrow is pointing. All images are set to the same scale, with the fundamental wavelength listed for each image in nm. Color scale represents normalized counts at the CCD.

Table 2.2Ca<sup>+</sup> Velocities. Wavelengths are vacuum, and direction of travel is either up or down in the plane of the page, parallel to the laser radiation.

Wavelength (nm)	Velocity (m s <sup>-1</sup> )	Direction of travel
786.9609	1731.3140	u
786.9603	1495.2246	u
786.9599	1337.8318	u
786.9595	1180.4393	u
786.9591	1023.0468	u
786.9585	786.9585	u
786.9581	629.5664	u
786.9574	393.4787	u
786.9570	236.0871	u
786.9564	0.0000	n/a
786.9560	157.3912	d
786.9554	393.4777	d
786.9550	550.8685	d
786.9543	786.9543	d
786.9539	944.3447	d
786.9535	1101.7349	d
786.9529	1337.8199	d
786.9525	1495.2097	d
786.9521	1652.5993	d
786.9517	1809.9888	d

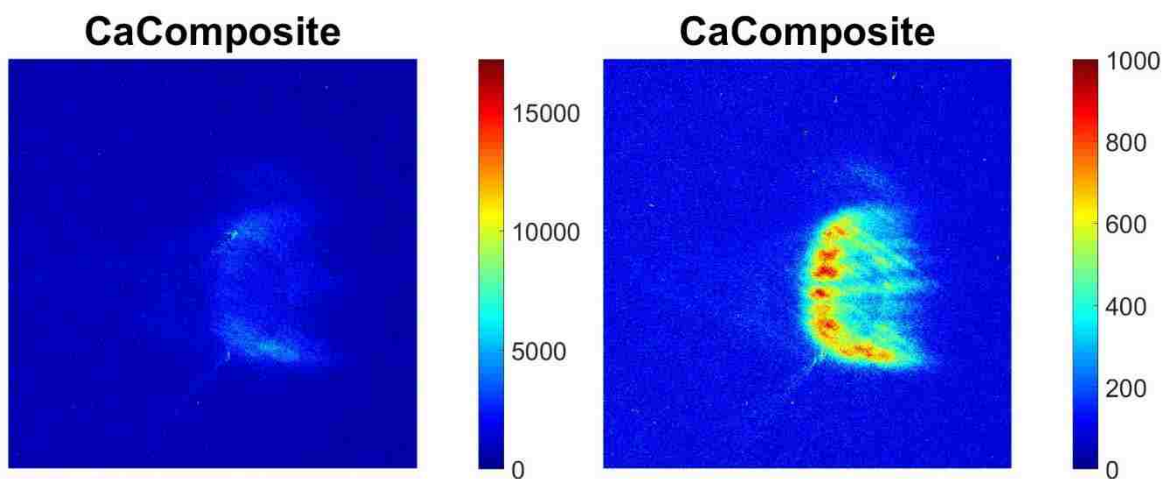


Figure 2.13 Total Ca ion beam with two processing methods. On the left the image is processed the same way as discussed with Ba. On the right, a different processing method compares two images at a time and for each pixel takes the most intense value of the two. This method is not a true summation but shows where we would expect to see ions and the general size of the ion beam. However, we lose the spatial relative intensity information. Color scale represents normalized counts at the CCD.

## 2.4 Conclusion

Comparing the Ca data to the Ba ion beam we see that the same effect is occurring. There are two distinct lobes of ion density rapidly converging as they approach the universal cell. The significance of this result is its disagreement with simulation data. While the simulation data cannot be presented in this thesis, it indicated a collimated beam would be centered on the entrance to the universal cell based on the applied voltages in the ion optics. The experimental data is needed to improve the simulation and provides a way to build better models and in turn more efficient instrumentation. Additionally, this work shows Ca and Ba ions while varied in mass follow a similar path through the ion optics, where Ca ions give a good indication of what the bulk sample is doing.

To the best of our knowledge we are the only group currently making these kinds of measurements. We have shown PLIF as a valuable method to non-invasively obtain velocity and spatial distributions of ion density in a working ICP-MS

## 2.5 References

1. Edmund, A. J.; Bergeson, S. D.; Lyon, M.; Taylor, N.; Kalinitchenko, I.; Farnsworth, P. B., *Spectrochim. Acta, Part B* 2012, *76*, 109-118.
2. Drever, R. W. P.; Hall, J. L.; Kowalski, F. V.; Hough, J.; Ford, G. M.; Munley, A. J.; Ward, H., *Applied Physics B-Photophysics and Laser Chemistry* 1983, *31*, 97-105.



### 3 BEAM EXPANSION IN THE THIRD VACUUM STAGE

#### 3.1 Introduction

In an ICP-MS the mass analyzer operates at a pressure of about  $10^{-6}$  torr, while samples are introduced at atmospheric pressure. The vacuum interface in an ICP-MS is designed to pass the plasma from atmospheric pressure to low pressure regions with minimal changes to its composition.<sup>1</sup> The vacuum interface typically consists of two extraction cones that separate the vacuum stages as discussed in section 1.1.1. The geometry and placement of the cones is critical to maximizing ion transport efficiency through the interface. The second cone in the interface is called a skimmer cone, see Figure 1.1. Only a small portion of the ion beam will actually pass through the skimmer cone.

A vacuum interface design with ideal skimming would result in a narrow, conical beam with a similar composition of atoms, ions, and electrons before and after the interface.<sup>2</sup> Additionally, heavy particles would have a narrow velocity distribution under ideal skimming conditions.<sup>2</sup> Deviations from ideal skimming include changes to plasma composition, wide velocity distributions, and shock formations resulting in a secondary beam expansions.<sup>3</sup> These effects can be problematic, especially if they are not accounted for downstream in the ion optics, and could result in a loss of sensitivity for a variety of samples.

The Perkin Elmer NexION ICP-MS is unique among commercial instruments in that it uses three extraction cones in the vacuum interface. The third cone is called the hyperskimmer

cone and is mounted directly behind the skimmer cone. The idea with this design is to minimize beam expansion behind the interface by reducing the vacuum pressure in three steps instead of two,<sup>4</sup> as can be seen in Figure 3.1. Thus, the NexION has an additional vacuum stage compared to other commercial instruments. The region where the beam shaping ion optics are located in the NexION is referred to as the third vacuum stage. For comparison, in other commercial instruments the ion optics region is referred to as the second vacuum stage.

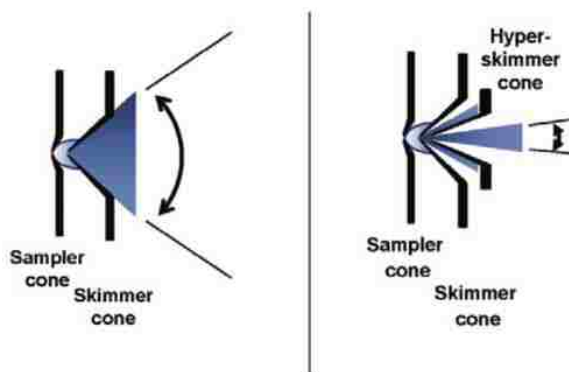


Figure 3.1 Figure and caption taken from reference 4. “The two-cone design on the left shows a wide ion beam divergence resulting from a single, large pressure reduction. The three-cone design on the right shows a small ion beam divergence, resulting from two small pressure reductions.”

In this chapter, the effect of a three-cone interface on ideal skimming is discussed. These experiments make up phase two of my research project. Specifically, the  $\text{Ba}^+$  ion is observed. A lighter mass ion,  $\text{Ca}^+$ , will be the subject of future work.

### 3.2 Experimental

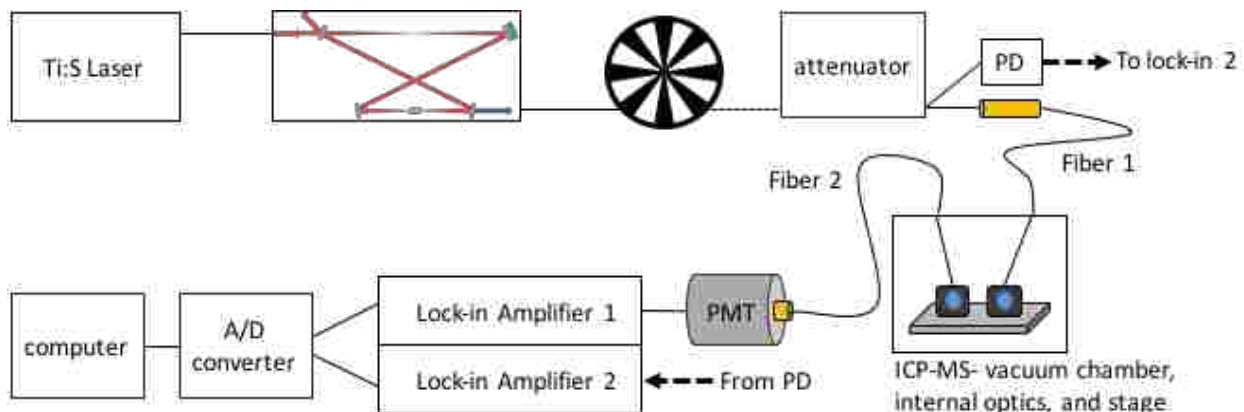


Figure 3.2 Experimental design overview.

An overview of the experimental setup can be seen in Figure 3.2. The same laser setup and frequency doubling cavity used in phase one are also used as the excitation source in phase two. The frequency doubled light passes through a chopper and is attenuated. Then the light is coupled to a fiber optic that carries the light inside the third vacuum stage of the ICP-MS. A saturation limit was determined to be above 10 mW of laser light entering the fiber optic, so the beam is attenuated to a power between 6-8 mW. An xy-translational stage holds the optics inside the instrument, where the y-axis is parallel to the path of the ion beam through the vacuum interface, and the x-axis defines side to side motion perpendicular to the y-axis. The z-axis is fixed, in that the stage cannot be moved up and down with respect to the y-axis. The light is aligned with the center axis of the vacuum interface in the z direction, but can be moved to different spatial points in both x and y. The light from the fiber optic is coupled to a lens system, on the translational stage, and focused to a point near the base of the hyperskimmer cone. A second set of lenses, focused to the same spot, collects any fluorescence and couples the light to a second fiber. The fiber sends the light back outside the ICP-MS to a photomultiplier tube,

PMT. The PMT signal is then sent to a lock-in amplifier. The signal matching the chopper frequency is detected and sent to an analog-to-digital converter with a USB connection. Finally, the converted signal is sent to a computer to be processed in LabVIEW and Matlab.

The setup also includes a photodiode (PD) to pick off a reflection of the laser beam after it has passed through the attenuator. The signal from the PD is sent to a second lock-in amplifier, and then converted with the same A/D converter. This signal serves as a reference for the laser power coming out of the frequency doubling cavity and is used to normalize the data when it is processed.

### 3.2.1 Instrumentation and Solutions

The same ICP-MS was used in the phase two experiments as was used in phase one, see section 2.2.1. However, several different modifications were made to the instrument that will be described in section 3.2.2. The same laser system was also used in phase two as was used in phase one. Please refer to section 2.2.2. The Ba solutions used in phase one, described in section 2.2.4, were also used in the phase two experiments.

### 3.2.2 ICP-MS Modifications

The vacuum chamber behind the three-cone interface is limited in space. To get a working optical system inside the ICP-MS was difficult, and required the removal of several hardware components of the instrument. The QID and universal cell were removed in order to open up more space in the vacuum chamber. The mass analyzer components were also removed. In order to keep the instrument operational, the voltages normally applied to the removed components were over ridden and remained off throughout the experiments. In short, the instrument ran with normal conditions through the vacuum interface, at which point the ion beam could expand into

third vacuum stage conditions without the influence of any electric fields. This allowed a free beam expansion to occur. The modifications also meant that mass counts could not be recorded, making it more difficult to account for instrument drift. The same set of sample introduction conditions were used for every data set in phase two, and are listed in table 3.1.

Table 3.1 Phase two ICP-MS operating parameters

Parameter	Value
ICP RF Power	1.6 kW
Nebulizer gas flow rate	0.94 L min <sup>-1</sup>
Auxiliary gas flow rate	1.20 L min <sup>-1</sup>
Plasma gas flow rate	18.00 L min <sup>-1</sup>
Peristaltic pump speed	20 rpm

A new lid was designed for the vacuum chamber in order to allow the fiber optics to pass light in and out of the vacuum chamber while the instrument was under vacuum. The lid also had to allow a way for the xy-translational stage to be manipulated without breaking vacuum. The new lid design can be seen in Figure 3.3. Two threaded holes were drilled in the center of the lid to couple national pipe tapered (NPT) fittings. The NPT fittings were adapted to Swagelok (Solon, OH) fittings and Teflon ferrules were used to create a seal around each fiber optic.

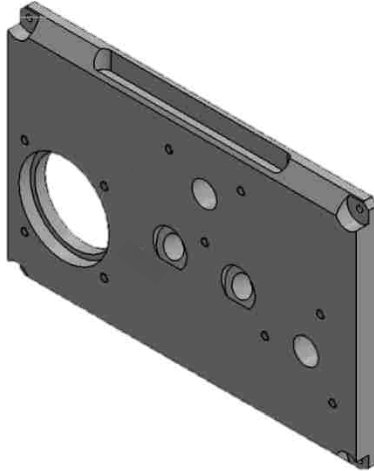


Figure 3.3 Modified vacuum chamber lid. Large hole on the left is a viewing window. Recessed holes, in center of plate, adapt to NPT fittings and allow fiber optics entry to vacuum system. Remaining holes on top and right side are for rotary feedthroughs to move the xy-stage. All small holes are for screws to mount brackets in place.

Vacuum- compatible, rotating feedthrough shafts were purchased that allowed the stage translators to be coupled to translators mounted on top of the vacuum chamber lid. The external translators were mounted in place with brackets and vacuum sealed with rubber O-rings. The lid design also included a window that allowed us to see inside the chamber.

### 3.2.3 Internal Optical Setup

The internal optical assembly was mounted directly to the chamber lid. The assembly is shown in Figure 3.4. Four poles were attached to the underside of the lid and held a baseplate in place. No part of the assembly touched the floor or walls of the vacuum chamber. The xy-translation stage was mounted to the baseplate, and the lens system was mounted to the stage. The entire assembly could be taken out of the instrument.

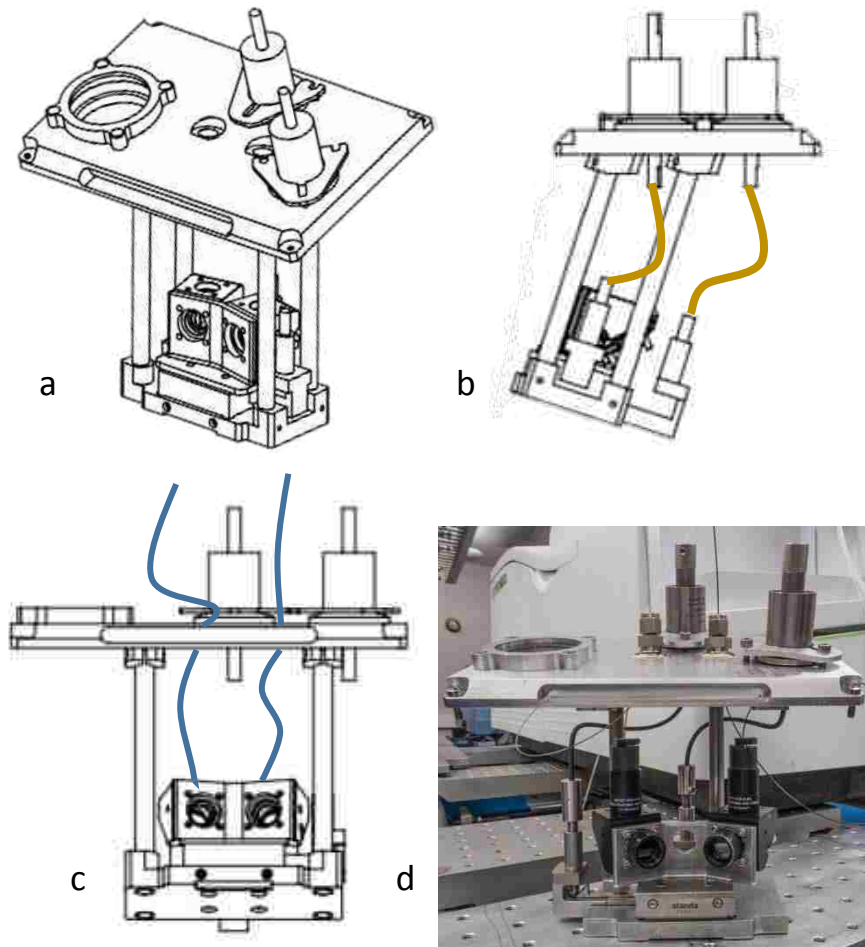


Figure 3.4 Internal optical assembly. (a) View of assembly and vacuum chamber lid as it would sit inside the vacuum chamber. (b) Cartoon of rotating shafts to move the xy-stage. (c) Cartoon of fiber optics coupled to lens system. (d) Photograph of the assembly.

The second frame, b, in Figure 3.4 shows a cartoon of where the rotating shafts were connected to both sets of translators. The third frame, c, shows where the fiber optics coupled to the system, and the fourth frame, d, is a photograph of the assembly while it is outside of the vacuum chamber. A close look at the fourth frame also shows how the fiber optics were looped in order to provide enough slack to move the stage without breaking the fibers.

The actual lens system consisted of two sets of lenses, mirrors, and windows. One set was to focus laser radiation at the base of the hyperskimmer cone. The second set was to collect the

fluorescence. In each set, a 45-degree mirror mount was attached to an aluminum bracket and held an elliptical mirror. It was necessary to wrap the sides of the elliptical mirrors with copper shim stock, as well as coat the back of each mirror with vacuum compatible thermal grease. A copper plate was also attached to the back of each mirror. These precautions were to provide thermal contact on each side of the mirror and to keep the temperature across the mirror surface uniform as the assembly was heated by the plasma. Without the copper and thermal grease, the surfaces of the mirrors developed a thermal gradient and cracked.

A 0.5-inch diameter lens with a 25-mm focal length, a spacer, and a custom-made fiber optic mount was attached to the top face of each mirror mount. On the front face of each mirror mount was another 0.5-inch diameter lens with a 50-mm focal length as well as a sapphire window. The windows were placed in front of the lenses to keep them clean. One set of lenses is shown in Figure 3.5, along with the fiber optic clamp.

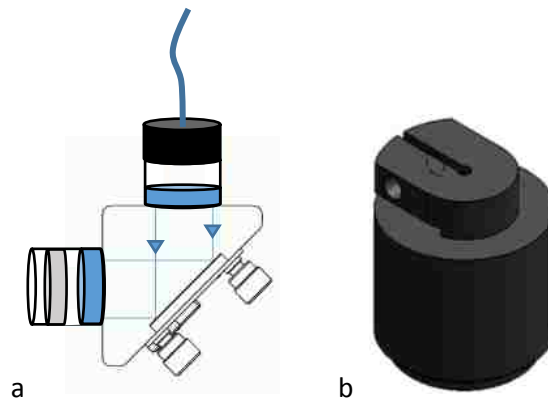


Figure 3.5 (a) Lens system for internal optics. Lenses are shown in blue, window in grey, and fiber optic clamp in black. The back wall of the mount holds an elliptical mirror which reflects the light 90 degrees. (b) Fiber optic clamp. A screw is used to pull the two wings of the clamp together and hold the fiber in place.

### 3.2.4 Data Processing

A LabVIEW script was written to be compatible with the information received from the National Instruments A/D converter. The script recorded data from both lock-in amplifiers,



wavelength data from high precision wavemeter, and time stamps. The values were saved to text files which were then processed in Matlab.

The Matlab script normalized the fluorescence signals for changes in laser power, and shifts in the baseline. Plots at every spatial position could be generated showing fluorescence as a function of wavelength. Then the peak fluorescence signal from each spatial position was saved, and a plot was generated showing peak intensity as a function of position. An example of the Matlab script is provided in Appendix B.

### 3.3 Results and Discussion

#### 3.3.1 Ba<sup>+</sup> Beam Expansion Profiles

Ba<sup>+</sup> beam expansion profiles are shown for two depth positions. The first depth is a cross section located 16.5 mm back from the tip of the hyperskimmer cone. The second depth is 18.5 mm back from the tip. The length of the hyperskimmer cone is 21.5 mm from tip to base, so these profiles are taken at cross sections within the cone. Figure 3.6 gives the fluorescence signal as a function of position at the 16.5 mm depth. The x-axis in the Figure shows where the spatial position was located relative to the center axis of the hyperskimmer, where 0 mm indicates the optics were centered on the axis. Figure 3.7 shows the same information for the 18.5 mm depth. At least 4 profiles were recorded for each depth. The data show that the Ba<sup>+</sup> ion beam is narrow and about the same width at both depth positions. The implication of the profiles is discussed in the following sections.

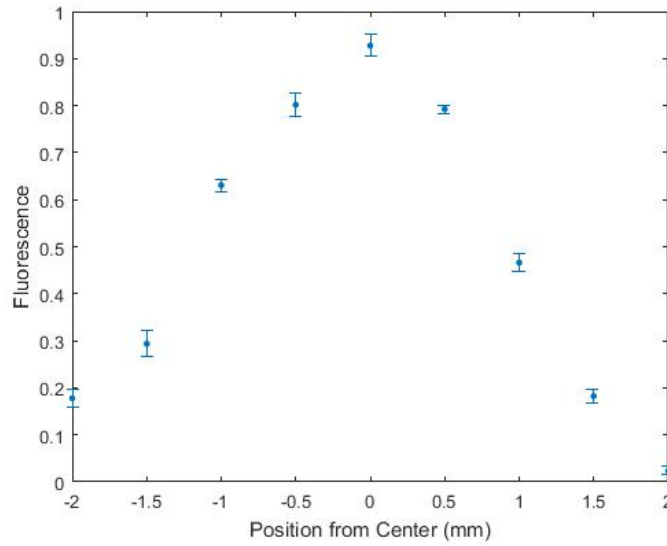


Figure 3.6 Fluorescence data as a function of spatial position. All data was taken at a depth of 16.5 mm behind the tip of the hyperskimmer cone. Optics were scanned left to right a total distance of 4 mm.

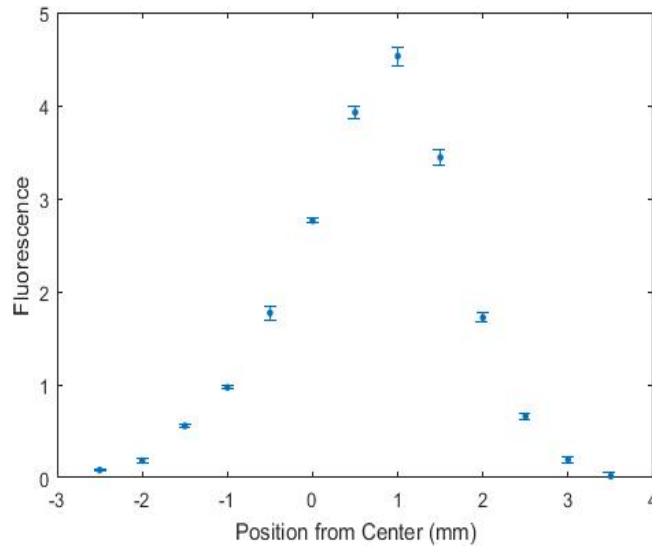


Figure 3.7 Fluorescence data as a function of spatial position. All data was taken at a depth of 18.5 mm behind the tip of the hyperskimmer cone. Optics were scanned left to right a total distance of 7 mm.

### 3.3.2 Optical Crossover Volume

To better understand the data presented in section 3.3.1, we first need to discuss the optical crossover volume. Before taking any measurements, the internal optics were mounted to

a stage outside of the instrument and focused onto a webcam. With both fibers backlit by lasers, the distance between the stage and the optics was varied until the beams were resolved on either extreme. The images can be seen in Figure 3.8. Note that the position of the webcam was rotated 90 degrees so the beams are actually crossing over from left to right, not up and down as the images suggest.



Figure 3.8 Cross over volume mapped onto a webcam. Both fibers were back lit and focused on a webcam. The distance between the optical assembly and the camera were varied incrementally until the two beams were resolved at either extreme. Images are rotated 90 degrees.

The images were imported into Photoshop and given hard edges so they could be identified as definite circles in Matlab. The region of overlap between the two beams was traced out in Matlab and placed on a spatial axis based on the distance traveled by the stage. This plot is shown in Figure 3.9. The stage traveled a total distance of 2 mm to resolve the beam on either end. The volume containing overlap region of the two beams was then calculated as  $0.53 \text{ mm}^3$ . This means that for each LIF point measurement, all the ions located within this volume are measured.

The overlap volume defines the spatial resolution of our measurement system. In simplest terms, the resolution in the x and z directions, perpendicular to the beam axis, is about 0.8 mm, a

dimension that results from the 2x image of the 0.4-mm optical fibers projected by both the excitation and collection optics. The resolution in the y direction, parallel to the beam axis, is about 2 mm, the length of the overlap region. A more-sophisticated analysis, developed by Dr. Farnsworth, shows that the instrumental broadening of the radial beam profiles is negligible. For the sake of completeness, I have included Dr. Farnsworth's analysis in section 3.3.3.

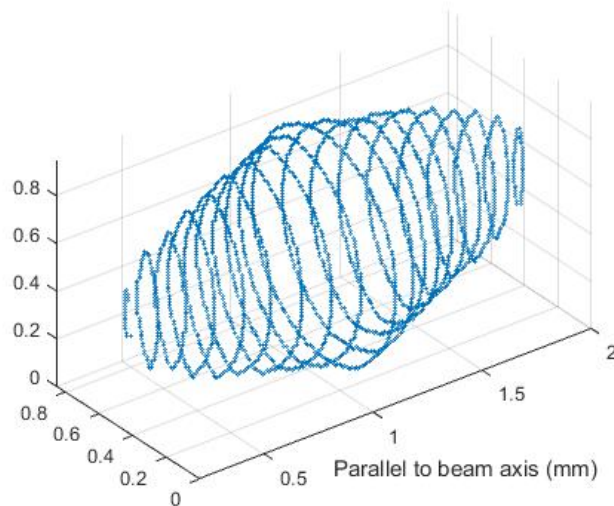


Figure 3.9 Crossover Volume calculated from webcam images. Y-axis is based on the distance traveled by the stage, and is parallel to the beam axis. X- and Z-axis represent the dimensions of the webcam. All axes are in mm.

### 3.3.3 Deconvolution of Beam Divergence Angle

To examine the effect of instrumental broadening on the measured beam profile, and to extract the actual beam profile from the experimental data, the beam was modeled as a section of a cone with a radius of 0.5 mm at the tip of the hyperskimmer. Given the Gaussian appearance of the experimental points, the beam was assumed to have a Gaussian radial cross section. The measured crossover volume and the model conical beam were numerically convoluted, varying the half angle defined by the cone axis and the edge of the cone until the calculated, convoluted profile matched the experimental data. The results are presented in Figure 3.10, where the circles

are the experimental data, the red trace is the conical density model, and the blue trace is the convoluted profile.

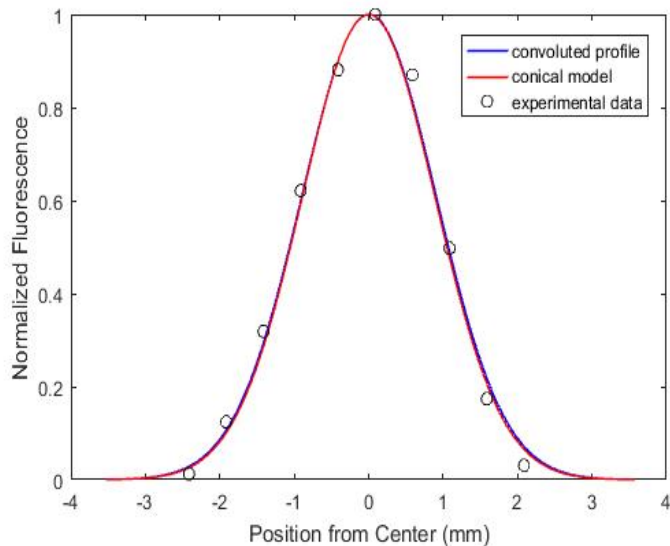


Figure 3.10 Beam Divergence angle comparison.

Two important conclusions can be drawn from this analysis: (1) the instrumental contribution to the measured beam width is negligible, and (2) the Gaussian radial profile assumed for the model beam is a good fit for the experimental data. The FWHM of the beam, measured 16.5 mm from the tip of the hyperskimmer, is 2.1 mm. This single set of measurements does not define the beam divergence, but as more data are acquired, we expect to be able to determine the divergence of the beam in addition to its width at a single point.

### 3.3.4 Instrument Drift and Hysteresis Effects

The performance of an ICP-MS drifts over time as components get dirty. In particular, running high concentrations of solution will inevitably cause clogging on the cones in the vacuum interface. As the cones clog, fewer ions pass into the third vacuum stage. In the phase

one experiments instrument drift could be accounted for by monitoring the mass counts at the mass analyzer. However, the mass analyzer has been removed for the phase two experiments and instrument drift is more difficult to correct.

Another factor affecting the results, comes from a hysteresis effect in the position of the xy-translational stage. The position of the stage was monitored by counting turns on control knobs mounted on the lid of the vacuum chamber. However, the nature of the flexible shafts that coupled the external knobs to the stage micrometers caused slight variations in position depending on how far they had been turned and in which direction they were being turned. There was also some inevitable variability in the placement of the lid that supported the optics as it was removed and replaced on the vacuum chamber. This variability resulted in slight shifts of the optical axes with respect to the axis defined by the hyperskimmer cone.

To account for instrument drift, shifts in the position of the optics, and any potential hysteresis effects we took replicate profiles and aligned their peaks. We observed peak shifts of less than one millimeter between runs, and it is reasonable to assume that the stage position could vary up to one millimeter due to the factors noted above. When the peaks are normalized to their maxima and shifted laterally to align the maxima, the profiles are reproducible. Hysteresis effects can be minimized if the stages are only moved in one direction, but reversal of direction introduces errors.

Figure 3.12 illustrates the combined effects of drift and hysteresis. The first frame shows the data uncorrected for hysteresis effects or instrument drift. The two runs displayed on the plot were taken consecutively, with the blue trace being the first run. The first trace was taken moving the stage from right to left relative to the direction of the optics. The second run was taken immediately following the first and was collected from left to right. We see that the

peak intensity has decreased on the second trace, which is expected to be observed as the cones become clogged. We also see that the spatial position where the peak intensity occurs has shifted. The second frame in the Figure shows the corrected profiles and we see that they are almost an exact match.

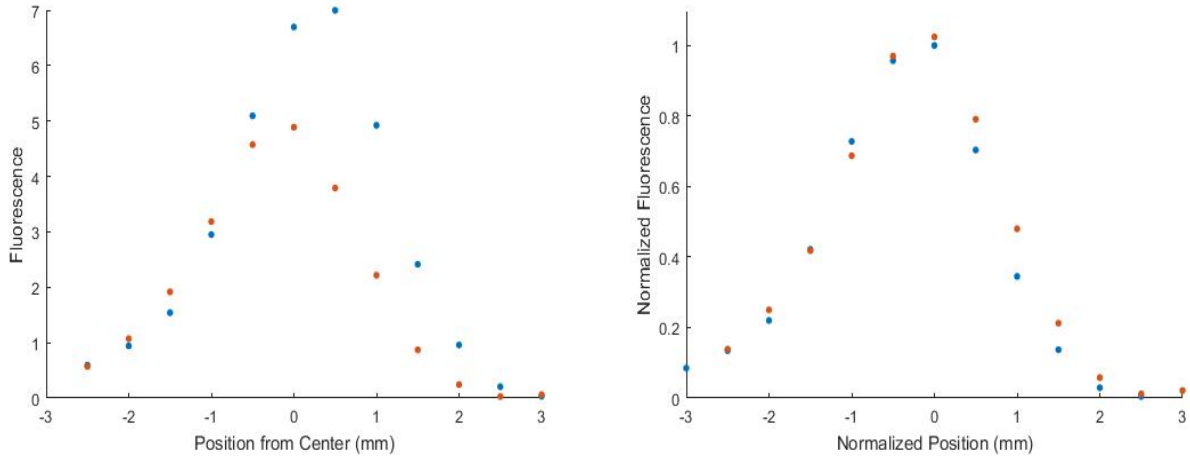


Figure 3.11. Beam profiles with and without corrections for instrument drift and hysteresis in stage position

When the same normalization steps are used to compare traces from the two depth profiles, 16.5 mm and 18.5 mm from the hyperskimmer tip, we see that there is no significant broadening of the ion beam. Figure 3.13 shows the normalized plot for the two depths. The FWHM of the beam profiles at each depth is the same within experimental error, indicating that the ion beam emerging from the tip of the hyperskimmer cone is narrow and well collimated.

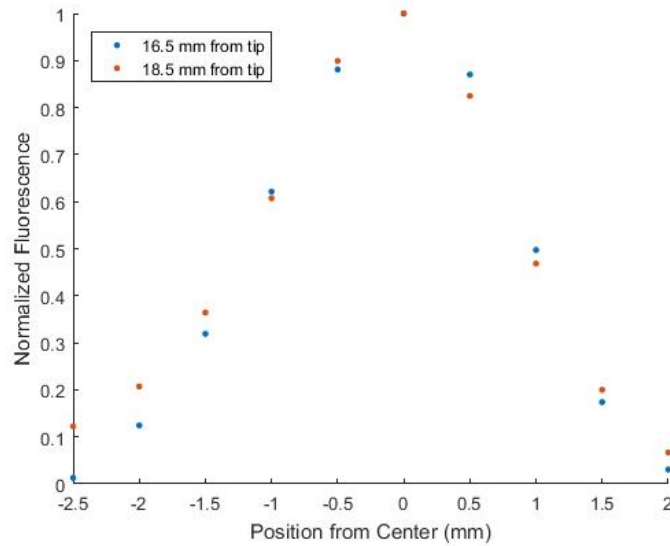


Figure 3.12. Normalized beam profiles at two depths

### 3.3.5 Evidence of Shock Structure

The final significant result from the beam profiles is an evidence of a shock structure forming at the tip of the hyperskimmer cone. On the individual traces, where signal is plotted as a function of wavelength, the wavelength was tuned over a broad range for every spatial point. An example of these traces is shown in Figure 3.14. These profiles are not Gaussian. The peaks are skewed and the peak wavelength shifts with changes in radial position. If ideal skimming were occurring we would expect each trace to follow a Gaussian profile, as was recorded by Radicic et al.<sup>5</sup> The individual traces show that skimming is not ideal for Ba<sup>+</sup> ion. Specifically, these traces indicate that there is a shock structure forming upstream from the measurement, most likely at the tip of the first skimmer cone. Shock structures generally lead to secondary beam expansions downstream.<sup>2-3</sup> Therefore, skimming for the Ba<sup>+</sup> ion is non-ideal.



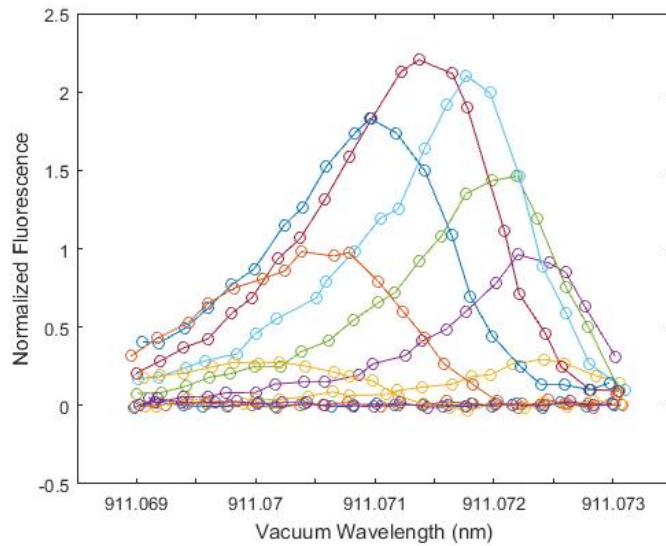


Figure 3.13 Evidence of shock structure formation at hyperskimmer tip. Fluorescence as a function of wavelength. Where each color represents a different spatial position along the base of the hyperskimmer cone. Profiles are skewed, non-Gaussian, and the peak wavelength is shifting.

### 3.4 Conclusion

The  $Ba^+$  ion beam profiles were recorded for two cross sections located at depths of 16.5 and 18.5 mm from the tip of the hyperskimmer cone. When normalized to a value of one, and corrected for hysteresis effects and shifts in the positions of the optics, the profiles at the two depths show no significant broadening of the ion beam. The FWHM of the ion beam was found to be 2.1 mm. There is evidence of a shock structure formation upstream of where the measurements were taking place. Overall, a three-cone vacuum interface yields a narrow, well-collimated ion beam at the two depths observed. However, ideal skimming for the  $Ba^+$  beam is not observed due to the formation of a shock somewhere in the interface.

### 3.5 References

1. Douglas, D. J.; French, J. B., *J. Anal. At. Spectrom.* 1988, 3, 743-747.
2. Taylor, N.; Farnsworth, P. B., *Spectrochim. Acta, Part B* 2012, 69, 2-8.
3. Niu, H. S.; Houk, R. S., *Spectrochim. Acta, Part B* 1994, 49, 1283-1303.
4. Elmer, P. The 30-Minute Guide to ICP-MS.  
[https://www.perkinelmer.com/CMSResources/Images/44-74849tch\\_icpmsthirtyminuteguide.pdf](https://www.perkinelmer.com/CMSResources/Images/44-74849tch_icpmsthirtyminuteguide.pdf).
5. Radicic, W. N.; Olsen, J. B.; Nielson, R. V.; Macedone, J. H.; Farnsworth, P. B., *Spectrochim. Acta, Part B* 2006, 61, 686-695.

## 4 FUTURE WORK

The following studies are suggested to add to the overall understanding gained from the work presented in this thesis.

### 4.1 Phase Two Calcium Study

The phase two experiments presented in chapter three were carried out using  $\text{Ba}^+$  as the analyte ion. Currently our research laboratory has the capability to frequency double the Ti:S laser to the wavelength needed in the fluorescence transition of two analytes,  $\text{Ba}^+$  and  $\text{Ca}^+$ . Of the two ions  $\text{Ca}^+$  more closely illustrates how the bulk composition of the plasma behaves because it has a similar mass to  $\text{Ar}^+$  ions. The predominant isotopes of Ar and Ca are  $^{40}\text{Ar}$  and  $^{40}\text{Ca}$ , with masses of 39.9624 amu and 39.9626, respectively.  $\text{Ba}^+$  is a more massive ion, where Ba atoms have an average atomic mass of 137.33 amu. Many studies have shown that matrix effects are mass dependent.<sup>1-6</sup> It has also been suggested that charge separation, and the onset of space charge effects, occurs within the skimmer cone.<sup>3,7</sup> Thus, we would expect Ca and Ba ion beams to behave differently as they expand into the third vacuum stage.

We chose to observe  $\text{Ba}^+$  first because it has a stronger fluorescence transition than  $\text{Ca}^+$ . Now that the details of the experiment have been worked out for an ion with strong fluorescence signals it should be fairly simple to adjust the experiment and observe  $\text{Ca}^+$ .

## 4.2 New Hyperskimmer Design

The second suggestion is of great interest to Perkin Elmer (Waltham, MA), who has funded this work. Based on simulations that they have performed, they have created a new design for the hyperskimmer that they think will give better overall transmission efficiency through their interface. We have already received a cone with the new design. Repeating the phase two experiments with the new hyperskimmer cone will be of great interest to the company and assist them in improving their simulation model. This work could be done for both  $\text{Ca}^+$  and  $\text{Ba}^+$ .

## 4.3 LIF point measurements at the tip of the Hyperskimmer

Finally, we have designed a second set of internal optics, see section 3.2.3, that would allow probing the ions closer to the tip of the hyperskimmer cone. The current setup is limited to probe only as close to the tip of the cone as 16.5 mm. The tradeoff between the two arrangements deals with the cross over volume as explained in section 3.3.2. Probing at the tip of the hyperskimmer requires the optics to cross at a more acute angle resulting in a longer crossover volume. This leads to poor axial resolution. However, it might be worth taking measurements at the hyperskimmer tip in an effort to observe shock structure formation.

#### 4.4 References

1. Edmund, A. J.; Bergeson, S. D.; Lyon, M.; Taylor, N.; Kalinitchenko, I.; Farnsworth, P. B., *Spectrochim. Acta, Part B* 2012, *76*, 109-118.
2. Stewart, II; Hensman, C. E.; Olesik, J. W., *Appl. Spectrosc.* 2000, *54*, 164-174.
3. Gillson, G. R.; Douglas, D. J.; Fulford, J. E.; Halligan, K. W.; Tanner, S. D., *Anal. Chem.* 1988, *60*, 1472-1474.
4. Tanner, S. D., *Spectrochim. Acta, Part B* 1992, *47*, 809-823.
5. Pupyshev, A. A.; Muzgin, V. N.; Lutsak, A. K., *J. Anal. At. Spectrom.* 1999, *14*, 1485-1492.
6. Larsen, J. J.; Edmund, A. J.; Farnsworth, P. B., *Spectrochim. Acta, Part B* 2016, *125*, 61-65.
7. Allen, L. A.; Leach, J. J.; Houk, R. S., *Anal. Chem.* 1997, *69*, 2384-2391.



## 5 APPENDIX A. PHASE ONE EXAMPLE MATLAB SCRIPT

### Clear Workspace

```
clear all
close all
```

### Import Dark Current File

```
FilenameD = 'darkALL.asc';
D = importdata(FilenameD);
Dark = D(:,(2:end));           %Removes indicator column
```

### Import Blank File

```
FilenameB = 'blank.asc';
B = importdata(FilenameB);
Blank = B(:,(2:end));         %Removes indicator column
blank_net = Blank-Dark;       %Removes Dark Current
rblank = blank_net(1345:1360,210:290); %Isolates reflection region
IntensityLaserBlank = mean2(rblank); %Averages reflection region values
```

### Import Velocity Distribution Files

```
%Imports all ascii files named according to the wavelength they were taken.
%For Ex 8085.asc corresponds to the image taken when the fundamental laser
%beam was 910.8085 nm
Filename1 = '8085.asc';
newData1 = importdata(Filename1);
Filename2 = '8090.asc';
newData2 = importdata(Filename2);
Filename3 = '8095.asc';
newData3 = importdata(Filename3);
Filename4 = '8100.asc';
newData4 = importdata(Filename4);
```

```

Filename5 = '8105.asc';
newData5 = importdata(Filename5);
Filename6 = '8110.asc';
newData6 = importdata(Filename6);
Filename7 = '8115.asc';
newData7 = importdata(Filename7);
Filename8 = '8120.asc';
newData8 = importdata(Filename8);
Filename9 = '8125.asc';
newData9 = importdata(Filename9);
Filename10 = '8130.asc';
newData10 = importdata(Filename10);
Filename11 = '8135.asc';
newData11 = importdata(Filename11);
Filename12 = '8140.asc';
newData12 = importdata(Filename12);
Filename13 = '8145.asc';
newData13 = importdata(Filename13);
Filename14 = '8150.asc';
newData14 = importdata(Filename14);
Filename15 = '8155.asc';
newData15 = importdata(Filename15);
Filename16 = '8160.asc';
newData16 = importdata(Filename16);
Filename17 = '8165.asc';
newData17 = importdata(Filename17);
Filename18 = '8170.asc';
newData18 = importdata(Filename18);
Filename19 = '8175.asc';
newData19 = importdata(Filename19);
Filename20 = '8180.asc';
newData20 = importdata(Filename20);

```

## Find Reflection Region to Normalize to Laser Power

```

%picks an arbitrary data file to be the reference for the final correction
%in the normalization loop below.
Reference_signal = newData18(:,(2:end));
%Removes Dark Current
Reference_signal_net = Reference_signal-Dark;
%Isolates reflection region
Refernece_region = Reference_signal_net(1335:1360,225:235);
%Averages reflection region values
Reference_point = mean2(Refernece_region);

```



## Organize Velocity Distribution into Data Cell

```
data(1).data=newData1;  
data(2).data=newData2;  
data(3).data=newData3;  
data(4).data=newData4;  
data(5).data=newData5;  
data(6).data=newData6;  
data(7).data=newData7;  
data(8).data=newData8;  
data(9).data=newData9;  
data(10).data=newData10;  
data(11).data=newData11;  
data(12).data=newData12;  
data(13).data=newData13;  
data(14).data=newData14;  
data(15).data=newData15;  
data(16).data=newData16;  
data(17).data=newData17;  
data(18).data=newData18;  
data(19).data=newData19;  
data(20).data=newData20;
```

Specify Laser Power to Normalize Between Two Different Data Sets. When no comparison is needed to between sets  $ALPD=ALPN$  so ratio is 1.

```
%average laser power denominator (in this case this is the reference)  
ALPD = 1;  
%average laser power numerator (in this case this is the current data set)  
ALPN = 1;
```

## Manually Type Average Mass Counts Corresponding to Each Image

```
MC1=230426.0668;  
MC2=219349.541;  
MC3=213338.7628;  
MC4=209072.858;  
MC5=207447.521;  
MC6=208501.1577;  
MC7=203161.9521;  
MC8=200612.9017;  
MC9=194399.0069;  
MC10=194457.9043;  
MC11=192858.283;
```

```
MC12=187530.472;  
MC13=186873.6807;  
MC14=186959.1255;  
MC15=184654.4823;  
MC16=184515.0407;  
MC17=182576.2061;  
MC18=181607.8875;  
MC19=180792.2276;  
MC20=179966.4888;
```

## Import Mass Counts to Data Cell

```
data(1).counts=MC1;  
data(2).counts=MC2;  
data(3).counts=MC3;  
data(4).counts=MC4;  
data(5).counts=MC5;  
data(6).counts=MC6;  
data(7).counts=MC7;  
data(8).counts=MC8;  
data(9).counts=MC9;  
data(10).counts=MC10;  
data(11).counts=MC11;  
data(12).counts=MC12;  
data(13).counts=MC13;  
data(14).counts=MC14;  
data(15).counts=MC15;  
data(16).counts=MC16;  
data(17).counts=MC17;  
data(18).counts=MC18;  
data(19).counts=MC19;  
data(20).counts=MC20;
```

## Laser Power Normalization for Loop

```
for i = 1:length(data)  
    x = data(i).data;  
    %Removes indicator column  
    signal = x(:,(2:end));  
    %Removes Dark Current  
    signal_net = signal-Dark;
```

```

%Isolates reflection region
reflection = signal_net(1335:1360,225:235);
%Averages reflection region values
IntensityLaserSignal = mean2(reflection);
%gives ratio of reflections
blank_multiplier = IntensityLaserSignal/IntensityLaserBlank;
%multiplies blank by reflection ratio & subtracts from the signal image
Signal_BS = signal_net-(blank_multiplier*blank_net);
%gives normalized image, multiplies signal by laser power ratio
normalized_image = Signal_BS*(Reference_point/IntensityLaserSignal);
ALPratio = ALPN/ALPD;
DSN = normalized_image.*ALPratio;
%Crops image
cropped = DSN(788:1299,:);
flipped_cropped = fliplr(cropped);
%stores images in cell
data(i).normalized = flipped_cropped;
end

```

## Mass Counts Normalization for Loop

```

for i= 1:length(data)
    w = data(i).normalized;
    y = data(i).counts;
    counts = w*(MC1);
    MCNormalized = counts/y;
    data(i).MCnormalized = MCNormalized;
end

```

## Create Image Files

```

scale = 30000;
T = 8085;
for ii = 1:length(data)
    xx = data(ii).MCnormalized; %recalls normalized data
    Y = 1:512; %sets axis dimensions
    X = 1:512; %sets axis dimensions
    Clow = 0; %sets lower limit on false color scale
    Chigh = scale; %sets upper limit on false color scale
    Clim = [Clow Chigh]; %gives false color scale, total
    figure
    imagesc(X,Y,xx,Clim); %turns ascii files into images
    colormap jet;
end

```

```

axis off
axis equal
colorbar('FontSize',20,'location','EastOutside');
title(['910.',num2str(T),' nm'],'FontSize',36);
T = T+5;
end

```

## Save Image Files

```

saveas(figure(1),'8085','jpg');
saveas(figure(2),'8090','jpg');
saveas(figure(3),'8095','jpg');
saveas(figure(4),'8100','jpg');
saveas(figure(5),'8105','jpg');
saveas(figure(6),'8110','jpg');
saveas(figure(7),'8115','jpg');
saveas(figure(8),'8120','jpg');
saveas(figure(9),'8125','jpg');
saveas(figure(10),'8130','jpg');
saveas(figure(11),'8135','jpg');
saveas(figure(12),'8140','jpg');
saveas(figure(13),'8145','jpg');
saveas(figure(14),'8150','jpg');
saveas(figure(15),'8155','jpg');
saveas(figure(16),'8160','jpg');
saveas(figure(17),'8165','jpg');
saveas(figure(18),'8170','jpg');
saveas(figure(19),'8175','jpg');
saveas(figure(20),'8180','jpg');

```

## Total Ion Beam Summation for Loop

```

nn = zeros(512, 512);
for n= 1:length(data)
    nn = nn+data(n).MCnormalized;
end

total_maxes = max(nn);
total_max = max(total_maxes);

```

## Total Ion Beam Alternative Summation for Loop

```

%Only one summation can be active at a time

```

```

% finimage=zeros(512,512);
% for n= 1:length(data);
%   nn = data(n).MCnormalized;
%   log1=nn>finimage;
%   log2=not(log1);
%   finimage=log1.*nn+log2.*finimage;
% end

```

## Create and Save Total Ion Beam Image

```

YY= 1:512;           %sets axis dimensions
XX= 1:512;           %sets axis dimensions
CLOW = 0;            %sets lower limit on false color scale
CHIGH = total_max;   %sets upper limit on false color scale
CLIM = [CLOW CHIGH]; %gives false color scale, total
figure
imagesc(XX,YY,nn,CLIM);
colormap jet;
title('BaComposite','FontSize',32);
colorbar('FontSize',20,'location','EastOutside');
axis off
axis equal
saveas(figure(21),'BaComposite','jpg');

```

## Import Orifice File and Create Image- to superimpose on total ion beam

```

ori = 'orifice.asc';
orifice = importdata(ori);
signal1 = orifice(:,(2:end));
croppedori = signal1(788:1299,:);
flipori = fliplr(croppedori);
figure
imagesc(flipori,[0 800]);
colormap bone;
title('Orifice','FontSize',32);
colorbar('FontSize',20,'location','EastOutside');
axis off
axis equal
saveas(figure(22),'ORIFICE','jpg');

```

## Import Target File and Create Image- to set scale

```

tar = 'target.asc';
target = importdata(tar);

```

```
signal2 = target(:,(2:end));  
croppedtar = signal2(788:1299,:);  
fliptar = fliplr(croppedtar);  
figure  
imagesc(fliptar,[0 1800]);  
colormap bone;  
axis off  
axis equal  
saveas(figure(23),'SCALE'.jpg);
```

*Published with MATLAB® R2016b*

## 6 APPENDIX B. PHASE TWO EXAMPLE MATLAB SCRIPT

The script contains one main for loop that iterates for every spatial position. Within the main loop are two additional loops. The first inner for loop averages together the five replicate runs taken every time the LabVIEW file is started. We also took triplicate measurements at each wavelength and the second inner for loop averages together the triplicate measurements. The wavelength plots are generated within the main loop. After the main loop the spatial plots are generated.

```
close all
clear all
% Import Data Files
NHeaderLines = 22;
f1='CBa2DS';
f2='_';
f3='.txt';
m=6; % Where m is the position and is included in the file name

for w = 1:24
    fname = strcat(f1,num2str(m),f2,num2str(w),f3);
    X = importdata(fname, ',', NHeaderLines);
    % [time wavemeter outputV LockinData1 LockinData2]
    time = X.data(:,1);
    Wavelength = X.data(:,2);
    OutputVoltage = X.data(:,3);
    PMTSignal = X.data(:,4);
    LPSignal = X.data(:,5);

    % Average Lock-In signal for each wavelength
    row = 1;

    for i = 1:5:(length(X.data)-4)
```

```
%F for fluorescence signals
```

```
F1 = PMTSignal(i);
```

```
F2 = PMTSignal(i+1);
```

```
F3 = PMTSignal(i+2);
```

```
F4 = PMTSignal(i+3);
```

```
F5 = PMTSignal(i+4);
```

```
FAverage = (F1+F2+F3+F4+F5)/5;
```

```
%LP for laser power factor
```

```
LP1 = LPSignal(i);
```

```
LP2 = LPSignal(i+1);
```

```
LP3 = LPSignal(i+2);
```

```
LP4 = LPSignal(i+3);
```

```
LP5 = LPSignal(i+4);
```

```
LPAverage = (LP1+LP2+LP3+LP4+LP5)/5;
```

```
%Normalization for laser power
```

```
GData(row,2) = FAverage/LPAverage;
```

```
% W for wavelength
```

```
W1 = Wavelength(i);
```

```
W2 = Wavelength(i+1);
```

```
W3 = Wavelength(i+2);
```

```
W4 = Wavelength(i+3);
```

```
W5 = Wavelength(i+4);
```

```
WAverage = (W1+W2+W3+W4+W5)/5;
```

```
GData(row,1) = WAverage;
```

```
% T for time
```

```
T1 = time(i);
```

```
T2 = time(i+1);
```

```
T3 = time(i+2);
```

```
T4 = time(i+3);
```

```
T5 = time(i+4);
```

```
TAverage = (T1+T2+T3+T4+T5)/5;
```

```
GData(row,3) = TAverage;
```

```
row = row+1;
```

```
end
```

```
figure
```

```
plot (GData(:,1), GData(:,2),'!');
```

```
ROW = 1;
```

```
for ii = 1:3:(length(GData)-11)
```

```
FF1 = GData(ii,2);
```

```
FF2 = GData(ii+1,2);
```



```

FF3 = GData(ii+2,2);
FFAverage = (FF1+FF2+FF3)/3;
GGData(ROW,2) = FFAverage;
FFStDev = (sqrt(((FF1-FFAverage)^2)+((FF2-FFAverage)^2)+((FF3-FFAverage)^2))/2);
GGData(ROW,3) = FFStDev;

WW1 = GData(ii,1);
WW2 = GData(ii+1,1);
WW3 = GData(ii+2,1);
WWAverage = (WW1+WW2+WW3)/3;
GGData(ROW,1) = WWAverage;

TT1 = GData(ii,3);
TT2 = GData(ii+1,3);
TT3 = GData(ii+2,3);
TTAverage = (TT1+TT2+TT3)/3;
GGData(ROW,4) = TTAverage;
ROW = ROW+1;
end

figure
plot (GGData(:,1), GGData(:,2),'.','Markersize', 10);
hold on

%Max is only good for the data column, NOT the wavelength column
[Max, MaxRow] = max(GGData);
Signal = Max(:,2);
SRow = MaxRow(:,2);
STFINAL = GGData(SRow,3);
TimeCorrection = GGData(SRow,4);
baseline = GGData(1:3,2);
Baseline = mean(baseline);
BaseStDev = (sqrt(((GData(1,2)-Baseline)^2)+((GData(2,2)-Baseline)^2)+((GData(3,2)-Baseline)^2)+((GData(4,2)-Baseline)^2)+((GData(5,2)-
Baseline)^2)+((GData(6,2)-Baseline)^2)+((GData(7,2)-Baseline)^2)+((GData(8,2)-Baseline)^2)+((GData(9,2)-Baseline)^2))/8);
FINAL = Signal-Baseline;
t(w) = TimeCorrection;
a(w)=FINAL;
s(w) = sqrt(STFINAL^2+BaseStDev^2);
end

TTT = t';
UUU = TTT(1:12,:);
VVV = TTT(13:24,:);

figure
hold on

```

```
AAAa = a(:,1:12);
AAAAb = a(:,13:24);
AAA = AAAa';
CCC = AAAAb';
b = [-2.5 -2 -1.5 -1 -0.5 0 0.5 1 1.5 2 2.5 3];
BBB = b';
SD = s';
plot(BBB,AAA,','MarkerSize',10);
plot(BBB,flipud(CCC),','MarkerSize',10);
hold off
figure
hold on
errorbar(BBB,AAA,SD(1:12,:),','MarkerSize',10);
errorbar(BBB,flipud(CCC),flipud(SD(13:24,:)),','MarkerSize',10);
```

*Published with MATLAB® R2016b*